Picosecond excitation and selective intramolecular rates in supersonic molecular beams. III. Photochemistry and rates of a charge transfer reaction

J. A. Syage, P. M. Felker,[a] and A. H. Zewail[b]
Arthur Amos Noyes Laboratory of Chemical Physics, California Institute of Technology, Pasadena, California 91125[c]

(Received 20 January 1984; accepted 13 March 1984)

The picosecond state-selective dynamics and photochemistry of the molecule A–$(CH_2)_3$–φ, where A and φ are aromatic chromophores, was studied under collision-free conditions in a supersonic beam. Time-resolved fluorescence measurements of the reactant and the charge transfer (exciplex) product were undertaken as a function of specific vibrational energy above the zero point level of S_1. From these studies along with an analysis of the excitation spectra, dispersed flourescence, and quantum yields, the following results and conclusions were reached: (i) IVR is much faster than reaction at all excess energies studied. (ii) The energy threshold for product formation is $E_0 \simeq 900\ cm^{-1}$ (2.6 kcal/mol). The analysis of the rates using an effective temperature model gives a frequency factor of $A_0 \approx 1.2 \times 10^{10}\ s^{-1}$. Four torsions were identified as critical to the reaction dynamics which were modeled according to a multidimensional reaction coordinate using an RRKM scheme. (iii) The thermodynamics of the isolated charge transfer product indicates strong stabilization $\Delta H = -9.2$ kcal/mol and extensive charge transfer, the static dipole moment is 13 D, and the charge transfer contribution to the total electronic wave function $|c_2|^2$ is 0.86. (iv) A comparison of the present work to solution phase studies of A–$(CH_2)_3$–φ indicates similar static properties but different dynamics. The calculated thermal (room temperature) reaction time for exciplex formation in the vapor (540 ps) was compared to the shortest observed value in solution (1.4 ns) to assess the role of the solvent on the chain motions which lead to product formation.

I. INTRODUCTION

In the first two papers of this series,[1,2] we presented an account of the investigation of intramolecular vibrational-energy redistribution (IVR) using the picosecond-jet method.[3,4] Understanding the selectiveness of IVR among different rotational-vibrational degrees of freedom and the effect of this redistribution on the overall dynamics of a molecule is a crucial concern in the study of selective photochemical processes in isolated molecules. Only recently have the measurements of such selective rates for photochemical changes (e.g., *trans–cis* isomerization of stilbene[5,6] and related systems[7,8]) been obtained using picosecond laser excitation of jet-cooled molecules. By exciting into specific single vibronic levels (SVL), it was possible to search for mode selective channels and measure the energy thresholds for these processes.[3] The rates for isomerization,[5–8] for instance, were measured by monitoring in time the population of the initially prepared state. However, the channelling of the population to *product* states following the IVR and the photochemistry could not be directly followed.

Recently, we communicated results[9] on a photochemical process which allowed us to monitor the formation of the product as a function of specific excess energy deposited in a single chromophore. The molecule studied was

$$A\text{–}CH_2\text{–}CH_2\text{–}CH_2\text{–}\phi,$$

where A stands for anthracene (*C*-9 substitution) and φ for *N*,*N*-dimethylaniline (*C*-4 substitution). In solution, this molecule upon local excitation in the anthryl group is known to undergo a conformational change promoted by solvent to form a strongly fluorescing charge transfer or exciplex state.[10–13] This process is particularly interesting when the molecule is jet cooled since the chain connecting the two chromophores has insufficient initial energy to undergo a change in geometry. Thus, the formation of the product or folded species (exciplex), which has a different fluorescence spectrum from anthracene (i.e., the "product" can be monitored separately from the "reactant"), must depend on IVR from anthryl modes into exciplex promoting modes. This paper gives a full account of the earlier communication[9] on the picosecond dynamics of this chromophore selective excitation in A–$(CH_2)_3$–φ.

In presenting the picosecond-jet results on A–$(CH_2)_3$–φ, we have two objectives in mind. First, we shall examine the dynamics of intermode coupling and their influence on the reaction rates. In particular, the following questions are of central focus: How selective is IVR in populating reactive vs nonreactive modes? What is the nature of the torsional chain modes and how do they participate in exciplex formation? How does the involvement of several chain modes along the reaction coordinate affect the rate of reaction?

Second, the photochemistry of the exciplex will be described and related to the kinetics, thermodynamics and potential energy surface for exciplex formation. In this study of intramolecular (charge transfer) photochemistry, we are interested in understanding the differences in the picosecond dynamics of exciplex formation under jet-cooled conditions

[a] IBM Research Fellow.
[b] Camille and Henry Dreyfus Foundation Teacher–Scholar.
[c] Contribution No. 6976.

 0021-9606/84/172233-24$02.10

compared to those reported under thermally congested bulb and solution conditions. Furthermore, by comparing our jet results with those for solution, we are able to examine the role of the solvent in the exciplex kinetics.

The paper is arranged as follows: Sec. II describes the experimental apparatus (picosecond laser-continuous jet and nanosecond laser-pulsed jet systems), data analysis, and materials. In Sec. III, we present our results and analysis on the vibrational structure of the ground and first excited electronic states of A–$(CH_2)_3$–φ and anthracene, as well as the time-resolved measurements and relative quantum yields as a function of excess energy. A discussion of the energy specific reaction dynamics of A–$(CH_2)_3$–φ is encompassed in Sec. IV. The section begins by examining the electronic and thermodynamic properties resulting from intramolecular energetics (hence no solvent interactions) (Sec. IV A). We then relate the measured rates to a kinetic model describing the reaction dynamics in the isolated molecule (Sec. IV B). Finally, an analysis of the intramolecular dynamics covering the details of IVR and the reactive torsional chain modes is discussed (Sec. IV C). There we focus on a model for a multidimenional reaction coordinate and discuss the ramifications of coupled reactive modes. Comparisons to the solution phase are also made where we examine the extent to which solvent molecules impede the motions of the reactive torsional modes.

II. EXPERIMENTAL

A. Nanosecond laser-pulsed jet apparatus

A pulsed supersonic jet system using nanosecond laser excitation was employed to record excitation and dispersed fluorescence spectra as well as time-resolved spectra involving long-lived (> 20 ns) decays.

The pulsed beam apparatus is a new home-built system which is diagrammed in Fig. 1. Central to the pulsing scheme is a pulse controller, designed to perform as a dual pulse generator and a pulsed amplifier. This device is used for triggering the pulsed beam nozzle, the YAG pumped dye laser, and a feedback system for automatic angle tuning of the KDP doubling crystal. The pulsed outputs are independently adjustable for pulse duration and delay. A digital display gives instant readouts of all trigger pulse widths and delays as well as repetition rate and total number of pulses.

The pulsed nozzle is activated by a low inductance solenoid which is driven by the pulsed amplifier capable of delivering greater than 10 kW of peak power. Amplified pulse durations of about 500 μs with $\approx$100 V and 100 A peak power worked well typically giving nozzle pulse widths of about 250 μs (FWHM). The mechanical delay inherent in activating the nozzle is about 600–800 μs depending on the amplified pulse and has a jitter and long term stability of $\leqslant$20 μs (well within the nozzle pulse width). Although, the nozzle can operate at repetition rates in excess of 50 Hz, we were limited by the YAG laser to 15 Hz.

The low duty cycle of our pulsed valve enables us to use a compact 4 in. diameter chamber which is pumped down by a 4 in. diffusion pump. The ambient pressure in the chamber during all experiments never exceeded 5×10^{-4} Torr.

We used a 300 μm aperture for all experiments reported here, although this dimension may be varied (750 μm maximum) by inserting appropriate electron microscope apertures. Cooling of the seed molecules in the jet was complete about 1.2 cm ($x/D = 40$) downstream from the nozzle as indicated by constant rotational bandwidths and hot band intensities at longer distances. The rotational and vibrational temperatures were difficult to determine accurately. T_{rot} requires a detailed knowledge of the rotational constants which are imprecise for this large molecule. Anthracene and A–$(CH_2)_3$–φ cooled to similar rotational temperatures (as judged by the bandwidths) under 50 psi of He or Ne ($T_{rot} \leqslant 3$K) although Ne cooled better at lower backing pressures. Vibrational temperatures were estimated for A–$(CH_2)_3$–φ by assuming a Boltzmann distribution for the 11 cm^{-1} mode hot band intensities (this is not necessarily the overall vibrational temperature as different molecular vibra-

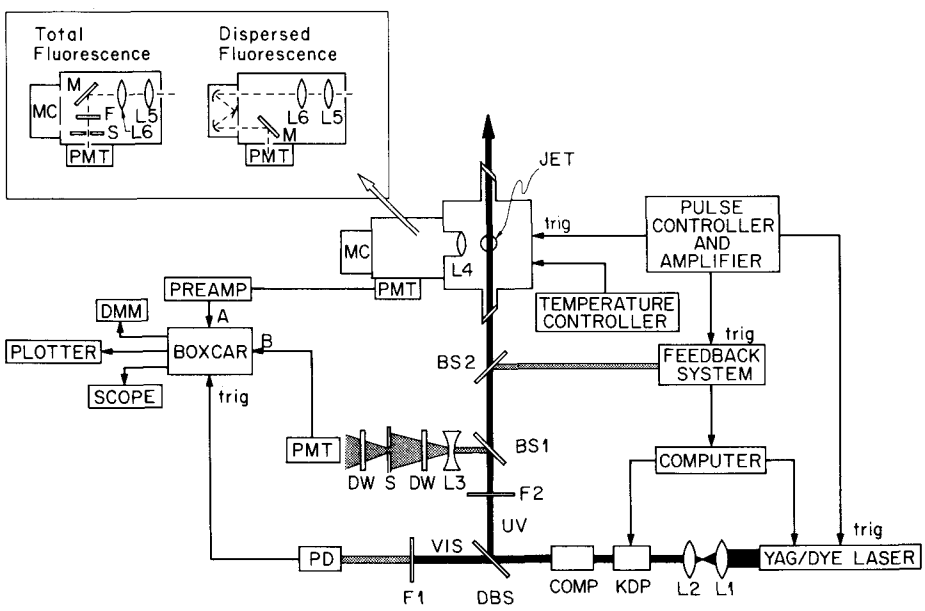

FIG. 1. Schematic of the nanosecond laser/pulsed jet apparatus. L—lens; F—filter; M—mirror; S—slit; BS—beam splitter; DBS—dichroic beam splitter; DW—diffusing window; MC—monochromator; COMP—compensator; DMM—digital multimeter; PD—photodiode; PMT—photomultiplier tube. The configuration of the detection optics are illustrated for recording dispersed and excitation (total) fluorescence spectra.

tions may cool to different extents). Under 50 psi of He and Ne, respectively, we obtained for A–$(CH_2)_3$–φ (11 cm^{-1} mode), $T_{vib} = 8$ and 6 K. A pressure of 50 psi N_2, on the other hand, failed to cool the 11 cm^{-1} mode of A–$(CH_2)_3$–φ satisfactorily ($T_{vib} \approx 20$ K). In anthracene, 50 psi N_2 proved to be an excellent vibrational cooler, but only a moderate rotational cooler as judged by the bandwidths. The vibrational cooling in A–$(CH_2)_3$–φ was comparatively better than in anthracene (except under N_2) possibly due to the low frequency vibrations. Ar was an efficient rotational and vibrational cooler for both molecules, but readily formed clusters with both molecules even at backing pressures of only 10 psi.

A digital temperature controller was used for heating the pulsed nozzle assembly via two 40 W cartridge heaters. The temperature was monitored by two chromel–alumel thermocouples, one located near the sample holder and the other near the heaters to detect any temperature gradients (typically less than a few °C). The stability of the temperature by this arrangement is better than 1 °C. Temperatures in excess of 200 °C may be attained, however, we used 120–130°C for anthracene and 150–165 °C for A–$(CH_2)_3$–φ.

The source of UV excitation in our experiments was a YAG pumped dye laser which was frequency doubled with a KDP crystal. The UV was then compensated for the beam walk which results from crystal rotation. A computer (Rockwell AIM 65) controlled feedback system (constructed in this laboratory[14]) maintains the optimum phase match angle of the KDP crystal as the laser wavelength is scanned. A dichroic beamsplitter is used to separate the visible (VIS) light from the UV light. The VIS portion is attenuated with a neutral density filter and used to trigger the boxcar integrator via a fast photodiode. The UV is filtered (Schott UG 11) to remove residual VIS and steered towards the beam apparatus. Two quartz plates are used as beamsplitters to divert a small portion ($\approx 10\%$) of the UV for monitoring by the KDP phase match feedback system and by a 1P28 photomultiplier. The output of the latter is fed into the *B* channel of a PAR 162/dual 164 boxcar and serves to normalize the fluorescence signal (*A* channel) for laser intensity variations resulting from shot-to-shot fluctuations, wavelength dependent dye output and long term drifts in power. To assure linearity of the 1P28, attenuating elements such as diffusing windows, a diverging lens and a pinhole were installed. The spectral response of the 1P28 is flat over the UV range we employed and hence no corrections were made.

The UV pulses enter and exit the beam apparatus through 8 in. long, 1 in. diameter cylindrical ports with Brewster angle quartz windows. No baffles were used since our gated detection method effectively eliminates detected stray room light. (We found that baffles, when not perfectly aligned, can introduce an appreciable amount of scattered laser light.)

The fluorescence was collected by an $f/1$ lens mounted in the chamber and imaged into a light tight optics housing configured to either collect total fluorescence (excitation spectra) or dispersed fluorescence using a monochromator (wavelength resolved fluorescence spectra). These two arrangements are diagrammed in Fig. 1. In both cases, two translatable lenses allow proper matching of the effective $f/$ number of the combined three lens system to the monochromator and to the PMT. The lens system and housing dimensions offer several notable benefits. The lens system, for instance, allows a variation of the imaged $f/$number without changing the image plane which is coincident with the monochromator entrance slit or the PMT surface depending on the housing configuration. L5 is a field lens which contains light collected by L4 which would otherwise be lost by divergence in a two lens system. Finally, the lenses were chosen so that L6 acts as an aperture or "stop" in the excitation region of the jet so that light originating outside of a 5–10 mm diameter collection area is not detected. This feature strongly discriminates against scattered laser light.

For excitation spectra, the imaged light was reflected by a mirror through a choice of filters and an adjustable slit before impinging on the PMT. The slit further reduces the fluorescence collection zone and was used only when the level of scattered light became pronounced. Anthracene fluorescence and anthracene-like fluorescence in A–$(CH_2)_3$–φ were collected through Schott GG395 and Corning 0–51 UV cutoff filters with a Corning 7–51 UV bandpass filter. The exciplex fluorescence from A–$(CH_2)_3$–φ was collected through Schott GG455 and GG435 cutoff filters and a Corning 5–61 bandpass filter. These filter combinations effectively isolated the two types of fluorescence from each other as well as minimized scattered laser light.

For recording dispersed fluorescence spectra, the slit and filters were removed and the mirror simply relocated as indicated in Fig. 1. An $f/8$ Jarrell–Ash 0.5 m monochromator was used with slit resolution down to 0.5 Å.

The output of the EMI 6256B PMT was fed into the boxcar integrator by way of a preamp (required only for dispersed fluorescence spectra). As remarked earlier, the fluorescence signal was normalized to the laser pulse intensity via the A/B ratio mode of the gated integrator. An oscilloscope and digital multimeter were used to monitor the *A* and *B* boxcar inputs and the integrated A/B output, respectively. The latter signal in turn was recorded on a strip chart recorder for excitation and dispersed fluorescence spectra and on an *x-y* recorder for time-resolved spectra. Special care was taken to insure that the PMT outputs were linear with incident photon flux and that the molecular transitions were not saturated by excessive laser power.

B. Picosecond laser-continuous supersonic jet apparatus

The picosecond/continuous jet apparatus has been described previously,[1–4] hence, we present only a brief account of the system here. The continuous jet apparatus is equipped with a 12 in. ring jet diffusion pump capable of maintaining 10^{-4} Torr ambient pressure during normal operation. The jet is excited with a picosecond dye laser, synchronously pumped by a mode-locked argon ion laser. The dye pulses were cavity dumped (repetition rate variable from 0.8 to 4 MHz) and frequency doubled with $LiIO_3$ to give UV pulses with temporal and frequency pulse widths of ≈ 15 ps and ≈ 0.4 Å, respectively.

Fluorescence was collected with right angle geometry and $f/1$ optics and was focussed onto the slit of a 0.5 m

monochromator. Single photons were detected with a fast photomultiplier (PMT). For frequency dispersed fluorescence spectra, PMT pulses were counted by a multichannel analyzer (MCA) operated in multichannel scalar (MCS) mode. Fluorescence decays were measured using time-correlated single photon counting. This technique relies on converting the time that a photon is emitted after laser excitation to a voltage signal via a time-to-amplitude (TAC) converter. Time-gated dispersed fluorescence spectra were obtained by using the MCA in MCS mode to count output pulses from the TAC as the monochromator was scanned. By setting upper and lower discriminator levels on the MCA, only TAC pulses having amplitudes within a given range were counted. Since the amplitude of such pulses directly corresponds to an elapsed time between laser excitation and photon detection, this amplitude gating is equivalent to time gating.

The compound A–$(CH_2)_3$–φ was heated to $\approx$200 °C and expanded through a 150 μm pinhole. All expansions in the continuous jet were backed by 30 psi He unless otherwise noted. Excitation of the jet cooled molecules by the picosecond pulses occurred typically 4 mm from the nozzle. No change in the fluorescence decay times was observed at longer distances indicating that collision-free conditions had been attained.

C. Treatment of data

The picosecond decay curves were treated using an iterative nonlinear least squares algorithm. The temporal response function of the system was obtained by recording the response of the laser pulse. The quality of the fits was uniformly excellent as judged by the reduced χ^2 values and the weighted residuals which display the point-by-point deviation of the experimental curve from the fitted curve.[2]

The nanosecond time-resolved spectra were corrected for baseline effects by subtracting a null spectrum recorded with the pulsed nozzle turned off. The corrected decay curves were then plotted logarithmically to extract the observed decay times. The *system* response time of 30 ns was much shorter than the measured decay times, hence no deconvolution was necessary.

The dye laser and monochromator wavelength scales were calibrated against the known Ne lines from a Fe–Ne discharge lamp. The laser calibration relied on optogalvanic detection in which a voltage change is induced at the lamp anode when the laser becomes resonant with certain Ne transitions. An accuracy of better than 0.1 Å ($\leqslant$1 cm^{-1}) was obtained by this method, thus allowing the assignments of all lines in the excitation spectra to better than 2 cm^{-1}. The monochromator was calibrated to about 0.5 Å by recording the dispersed fluorescence spectrum of the Fe–Ne lamp. The assignments of the dispersed fluorescence lines of A–$(CH_2)_3$–φ, however, were limited by the monochromator slit resolution to about 5–10 cm^{-1}. No vacuum corrections were applied to assigned frequencies in excitation or fluorescence spectra.

The relative quantum yield data were obtained by taking the ratios of the integrated fluorescence signals for exciplex and anthracene-like emission. The integration was accomplished by weighing cutouts of the appropriate signals in the dispersed fluorescence spectra. Since the exciplex and anthracene-like emission are well separated in wavelength, problems associated with overlap were minimal. The combined monochromator and PMT spectral response was determined by recording the response of a calibrated 1000 W tungsten lamp. The observed response curve, in turn, was used to correct the intensities of all dispersed fluorescence spectra employed in the relative quantum yield determinations. The actual spectral response correction was minor.

The solution phase samples used to record fluorescence spectra were excited with a Hg lamp emitting at 3670 Å. The observed spectra (Fig. 14) are displayed without correction for the spectral response of the system, however, all analyses based on these spectra have incorporated the necessary corrections.

D. Materials

Scintillation grade anthracene was recrystallized twice from CCl_4. The purity, as checked by gas chromotography (gc), was 99.5%. The 9-methylanthracene (Alfa, 99%) was found to be 97.5% pure by gc and used as is. The 9-hexylanthracene was obtained from the University of Bordeaux, courtesy of the organic chemistry group. The purity following recrystallization in CCl_4 was 95% (the major impurity was anthracene; 4.5%).

The compound 1-(9-anthryl)-3-(4-*N*,*N*-dimethylaniline) propane (i.e., A–$(CH_2)_3$–φ) was prepared by a new synthetic route. The only other reported synthesis of A–$(CH_2)_3$–φ[12(a)] gives low yield and side products. Due to the large consumption of material in continuous jets ($\approx$100 mg per day depending on temperature), we developed an efficient synthetic scheme described in the Appendix. The identity of the compound A–$(CH_2)_3$–φ was confirmed by NMR, IR, UV–VIS absorption and emission spectroscopy, elemental analysis, and melting point determination. The purity following two recrystallizations in ethanol was 99% by gc.

Solution phase samples of A–$(CH_2)_3$–φ were prepared by repeated (at least five) freeze–pump–thaw cycles to remove oxygen and other fluorescence quenchers. Spectral quality solvents were used in all cases.

III. RESULTS AND ANALYSIS

A Jet-cooled excitation spectra

Our interest in A–$(CH_2)_3$–φ focuses on how single vibronic level (SVL) excitation in one part of a molecule followed by IVR can lead to molecular changes in another part of the molecule. To address this issue, we have undertaken a detailed analysis of the important vibrations (particularly the SVL's being excited) of the model molecule and compared with other anthracene derivatives. This pursuit entailed recording and analyzing the jet-cooled excitation spectra for 9-methylanthracene, 9-hexylanthracene, and A–$(CH_2)_3$–φ and relating them to the anthracene spectrum.

1. Symmetry assignments

The excitation spectra of A–$(CH_2)_3$–φ and anthracene are displayed in Figs. 2 and 3, respectively, and their as-

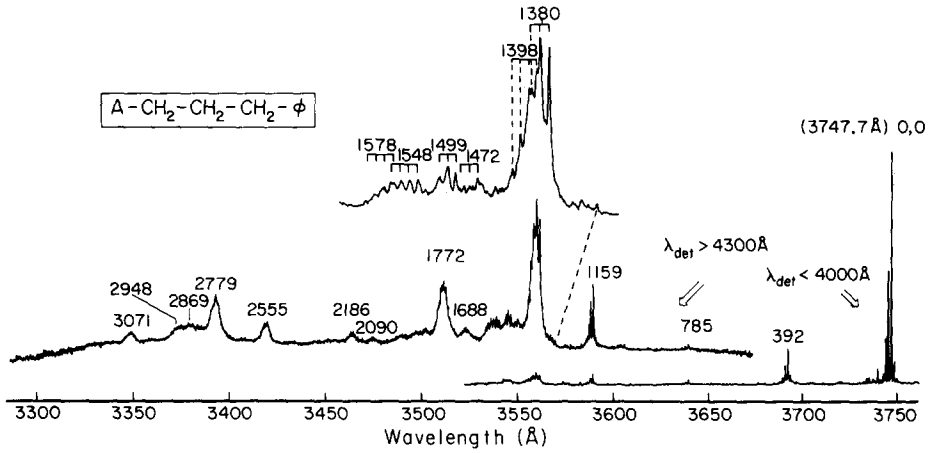

FIG. 2. Excitation spectrum of A–$(CH_2)_3$–φ under two different fluorescence detection conditions: $\lambda_{det} < 4000$ Å monitors only locally excited anthryl-type fluorescence, whereas $\lambda_{det} > 4300$ Å detects only exciplex fluorescence. The 1400 cm^{-1} region is enlarged showing the tentative assignments of these modes and the strong 11 cm^{-1} combinations. Sample temperature and backing pressure were 160 °C and 50 psi Ne, respectively.

signed frequencies and symmetries in Table I. The excitation spectra of 9-methyl and 9-hexylanthracene are similar to that of anthracene and are illustrated in Fig. 4. In D_{2h} point group, the $B_{2u} \leftarrow A_g$ electronic transition in anthracene is short axis (y axis) polarized (see Lambert, *et al.*[15] and references therein for details). In the Born–Oppenheimer and Condon approximations, only totally symmetric a_g vibrations are allowed because of Franck–Condon and symmetry considerations. A small vibronic interaction (Herzberg–Teller) involving B_{2u} with the higher excited electronic state B_{3u} however, introduces some b_{1g} activity into the anthracene spectrum.[15,16]

In subsequent text, we shall be referring to the transition from the zero point energies of the ground and first excited electronic states as the 0,0 or 0_0^0 transition. Reference to the zero point vibrational level of the excited electronic state will often be denoted as 0°. The 0_0^0 transition wavelengths for A–$(CH_2)_3$–φ and related compounds are given in Figs. 2–4 and summarized in Table III.

2. The 11 cm^{-1} mode

One of the interesting features in the A–$(CH_2)_3$–φ excitation spectra is the presence of an 11 cm^{-1} interval (Fig. 5). One would expect low frequency modes in this molecule as a result of torsional and bending motions in the propyl chain. It is perhaps surprising, however, that this and only this chain mode has such strong optical activity. A low frequency interval of 12 cm^{-1} is also observed in 9-hexylanthracene although the relative intensities are different. Interestingly, low frequency chain modes are not evident in the jet-cooled excitation spectra of hexylbenzene.[17]

One plausible suggestion for this low frequency vibration is a "crankshaft" type motion[18] whereby the aromatic end groups remain relatively fixed due to inertia and the elongated chain undergoes a symmetric back-and-forth twisting motion. Such motion is best visualized with molecular models and is expected to occur in chain molecules with heavy end groups.[18,19] Other three bond motions[20] which also leave the end groups stationary may be postulated although they are not symmetric with respect to the anthracene group. These types of motions are not unlike the ring flip which occurs in cyclohexane.

Another possible assignment for the 11 cm^{-1} mode is that of a torsion of the anthryl group about the chain substituent. We examine whether our measured frequency is consistent with that predicted for the anthryl torsion by resorting to a simple model outlined in Sec. IV C 1. The potential associated with internal rotation for symmetric harmonic motion may be expressed as

$$V(\alpha) = \tfrac{1}{2} V_N (1 - \cos N\alpha), \tag{1}$$

where V_N is the barrier height between minima and N is the number of minima.[21–23] For our purpose we assume a symmetric twofold (i.e., $N = 2$) potential arising from the rota-

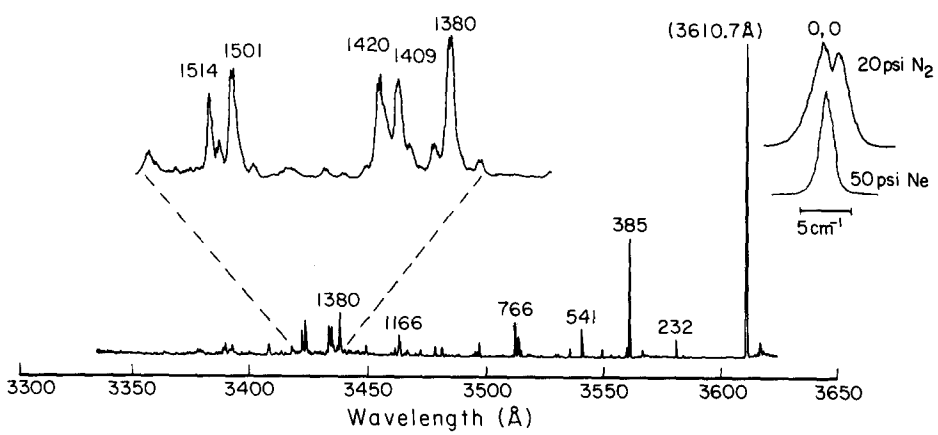

FIG. 3. Excitation spectrum of anthracene. The rotational bandshape of the 0,0 is illustrated under two different cooling conditions. Sample temperature was 130 °C and backing pressure 50 psi N_2.

TABLE I. Assignment of the excitation spectra of A–$(CH_2)_3$–φ and anthracene.

A–$(CH_2)_3$–φ			Anthracene		
Frequency[a] (cm^{-1})	Relative intensity[b]	Assignment[c]	Frequency[a] (cm^{-1})	Relative intensity	Assignment and symmetry[d]
0	100	origin	0	100	origin
11.1	50				
21.7	19	2×11			
32.2	4	3×11			
42	1	4×11			
52	6				
63	2	52 + 11			
69	3				
85	4				
96	3	85 + 11			
189	2				
199	1	189 + 11			
209		189 + 2×11			
			232	3	b_{1g}
392	15		385	31	a_g
401	8	392 + 11			
403	3				
			473	2	b_{1g}
			541	5	
			583	2	a_g
			755	4	a_g
785	2	2×392	766	8	2×385
796	1	2×392 + 11			
			889	2	b_{1g}
			1019	2	a_g
1159			1168	5	a_g
1170		1159 + 11			
1181		1159 + 2×11			
1191		1159 + 3×11			
			1184	1	b_{1g}
1210		1159 + 52			
1380			1380	12	a_g
1391		1380 + 11			
1393			1389	2	
1402		1380 + 2×11			
1405		1393 + 11			
1416		1393 + 2×11			
1426		1393 + 3×11			
			1409	7	b_{1g}
			1420	7	a_g
1472					
1483		1472 + 11			
1494		1472 + 2×11			
1499			1501	10	a_g
1510		1499 + 11			
1520		1499 + 2×11			
			1514	6	b_{1g}
1548		1159 + 392	1550	2	1168 + 385
1559		1159 + 392 + 11			
1571		1159 + 392 + 2×11			
1578					
1581		1159 + 392 + 3×11			
1590		1578 + 11			
1599		1578 + 2×11			
1609		1578 + 3×11			
1688			1635	2	b_{1g}?
1772		1380 + 392	1767	2	1380 + 385
1781		1380 + 392 + 11			
1789		1380 + 392 + 2×11			
			1792	3	1409 + 385
			1801	2	1420 + 385

TABLE I (*continued*).

A–$(CH_2)_3$–φ			Anthracene		
Frequency[a] (cm^{-1})	Relative intensity[b]	Assignment[c]	Frequency[a] (cm^{-1})	Relative intensity	Assignment and symmetry[d]
2090					
2186		$1380 + 2\times392 + n\times11$			
2555		$1380 + 11591 + n\times11$			
2779		$2\times1380 + n\times11$			
2869		$1499 + 1380 + n\times11$			
2948		$1380 + 1159 + 392 + n\times11$ and $1578 + 1380 + n\times11$			
3071		$2\times1380 + 392 + n\times11$			

[a] Frequencies are reported relative to the 0_0^0 to an accuracy of 2 cm^{-1}.

[b] Relative intensities are not reported for frequencies of 1159 cm^{-1} and greater since fluorescence is predominantly emitted from the exciplex state and detected with a different set of filters. Hence, the detected intensities do not bear a simple relationship to the 0_0^0 fluorescence intensity.

[c] Symmetries of fundamentals may be associated with those reported for anthracene for D_{2h} geometry. Combination bands involving an unresolved 11 cm^{-1} progression are designated by $n\times11$.

[d] Symmetry assignments are from Ref. 15.

tion of the chain through the plane of the anthryl group. One obtains for the torsional frequency[21]

$$\nu_T = N\sqrt{\frac{V_N B_1 B_2}{B}}, \tag{2}$$

where B_1 and B_2 are the rotational constants corresponding to the moments of inertia I_1 and I_2 of the two parts of the molecule about the torsional axis and B is the rotational constant for the sum of the moments $I_1 + I_2$. We associate B_1 with the anthryl group and obtain a value of 1.51×10^{-2} cm^{-1} for rotation about the short axis. The value of B_2 for the remaining segment of A–$(CH_2)_3$–φ is far more tedious to determine, particularly since it is dependent on the conformation of the molecule. Using molecular models we evaluated B_2 for two stable conformers of A–$(CH_2)_3$–φ (see Fig. 17) and obtained values of 0.62×10^{-2} (for tt) and 0.76×10^{-2} cm^{-1} (for $g^{\pm}t$).

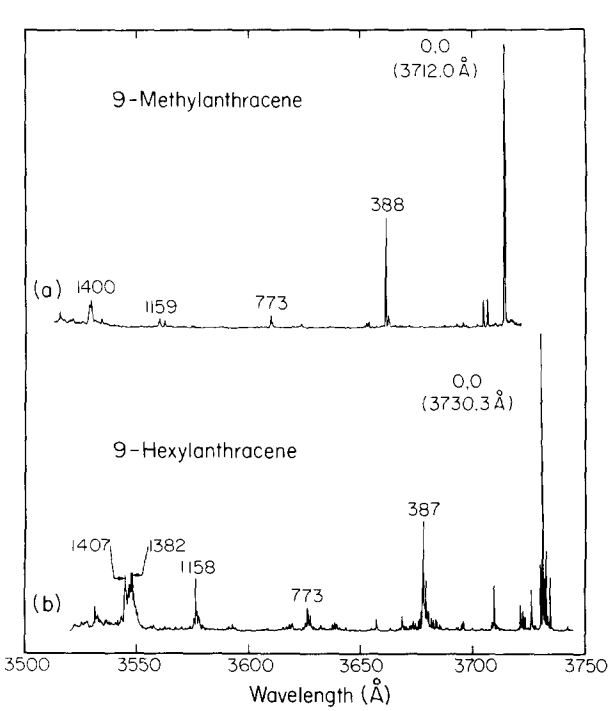

FIG. 4. Excitation spectra of (a) 9-Methylanthracene; 50 psi He, 140 °C and (b) 9-Hexylanthracene; 50 psi Ne, 160 °C.

An estimate of the barrier height for the anthryl internal rotation can now be made if we assume for the moment that the 11 cm^{-1} mode corresponds to this torsion. In this manner, we obtain the reasonable potentials of $V_2 = 1430$ (tt) and 1330 cm^{-1} ($g^{\pm}t$). More exact calculations including anharmonicities and higher order components on the potential surface[23] would lower these values somewhat [cf. Eqs. (17) and (18)]. Although methyl rotation in toluene has a barrier of only 5 cm^{-1},[24] the presence of an alkyl group in place of a hydrogen raises the barrier significantly. For instance, estimates on the Ph–C barrier in ethylbenzene range from about 400 to 600 cm^{-1}.[25,26] For longer chains interacting with larger aromatics (e.g., anthryl instead of phenyl), the barrier is expected to be even larger, in support of our calculations. Other evidence favoring the assignment of the 11 cm^{-1} mode to the anthryl torsion is found in the observed low frequency intervals of 12 cm^{-1} in 9-hexylanthracene [Fig. 4(b)] and 12 and 16 cm^{-1} in bianthryl.[27] By similarly assuming a twofold potential of $V_2 = 1400$ cm^{-1} for these compounds (probably not a good assumption for bianthryl), one calculates for the anthryl torsion, frequencies of 17 and 15 cm^{-1}, respectively.

An optically active mode extending throughout the chain has important implications regarding exciplex formation since it can act as a direct channel for funneling initially excited vibrational energy into the chain, thus promoting exciplex formation. We investigated this possibility by measuring the rate of exciplex formation for the 1159 mode and its 11 cm^{-1} progression [Fig. 5(c)] on the premise that the rate might be dependent on the number of 11 cm^{-1} quanta excited. We observed only a slight change in lifetimes (4.4,

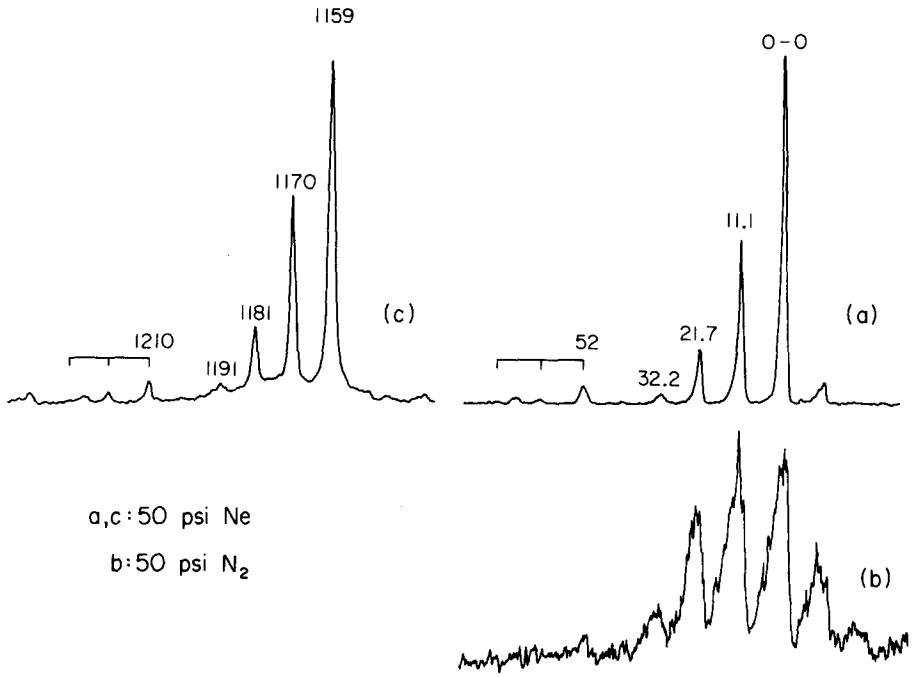

FIG. 5. High resolution excitation spectra of the 11 cm^{-1} progression in A–$(CH_2)_3$–φ; (a) 0,0 region (50 psi Ne), (b) 0,0 region (50 psi N_2) and (c) 1200 cm^{-1} region (50 psi Ne). We make note of the 52 cm^{-1} band.

4.3, 4.2, and 4.2 ns, respectively, for bands $1159 + n \times 11$ cm^{-1}, where $n = 0$–3) most likely attributable to excess energy rather than mode specificity.

3. Ground state conformations and exciplex spectra

Solution phase investigations of A–$(CH_2)_3$–φ[13] and other exciplex forming molecules[28] indicate that more than one ground state conformer may be present with very different propensities for forming exciplexes. It has been known for some time that chain molecules can exist in a number of different conformations. An example for the existence of different conformers of chain molecules with an aromatic substituent is found in the work of Smalley on jet-cooled alkylbenzenes.[17] For substituents of propyl length and longer, the excitation spectra show a doubling of lines with a displacement ranging from about 50 to 70 cm^{-1}. We failed to observe any obvious doubling pattern in the excitation spectra of 9-hexylanthracene and A–$(CH_2)_3$–φ as far as 300 cm^{-1} to lower energy of the 0_0^0 bands. There are, however, some indication for a weak second conformer in jet-cooled A–$(CH_2)_3$–φ. We have observed weak features 52 cm^{-1} to the blue of the major excitation lines. One cannot rule out the possibility that these lines represent a 52 cm^{-1} fundamental that forms strong combinations with other modes, however, their time dependence (discussed in Sec. III D) is consistent with that of another conformer.

It is possible that a thermal distribution of conformers will not be observed in the jet-cooled molecules if the distribution equilibrates during the course of the expansion (i.e., thermodynamic cooling). If on the other hand, cooling is sufficiently rapid (i.e., kinetic cooling), the jet expansion will *freeze in* a distribution of conformers corresponding to a higher temperature than that of the jet. For the moment, we assume the latter case and attribute the relative intensities of the 52 cm^{-1} and the 0_0^0 band to the ratio of conformers at the preexpansion temperature of 433 K. According to a Boltzmann distribution, this would correspond to an endothermicity for the unfavored conformer of nearly 800 cm^{-1}. If some thermodynamic cooling occurs, then the ratio of conformers would be associated with a lower temperature and be consistent with a smaller endothermicity.

Finally, we remark on the effects of exciplex formation on the excitation spectra of A–$(CH_2)_3$–φ displayed in Fig. 2. The fluorescence from the exciplex (Fig. 7) is shifted considerably from that of the anthracene moiety. We, therefore recorded the excitation spectra of A–$(CH_2)_3$–φ by collecting exclusively either exciplex ($\lambda_{det} > 4300$ Å) or anthracene-like fluorescence ($\lambda_{det} < 4000$ Å) by the procedure outlined in Sec. II B. One clearly sees a crossing region at about 1000 cm^{-1} from the 0,0 where the anthracene-like fluorescence falls off sharply and the exciplex fluorescence builds up. In the region below 2000 cm^{-1}, the lines in excitation are still relatively sharp, however, this structure disappears at higher energies. We observed a similar effect in the excitation spectrum of jet-cooled *t*-stilbene[6] and diphenylbutadiene[7] where the measured decays of the diffuse lines[5] indeed showed accelerated rates as a function of excess excitation energy due to isomerization.

B. Jet cooled fluorescence spectra

The assignment of the dispersed fluorescence spectrum of A–$(CH_2)_3$–φ in Fig. 6 clearly shows a close correspondence to that of anthracene (Table II). The frequencies measured for the fundamentals in A–$(CH_2)_3$–φ typically agree (within the experimental uncertainty of $\approx 5 - 10$ cm^{-1}) of their counterparts in anthracene. The symmetries attributed to the anthracene modes in Table II are discussed in a previous paper.[15]

There are a few low frequency modes that appear in the dispersed fluorescence spectrum of A–$(CH_2)_3$–φ that are absent in anthracene. The only one of these that may be posi-

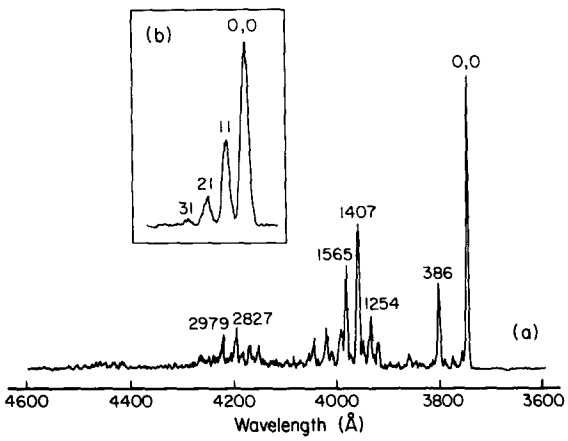

FIG. 6. Dispersed fluorescence spectrum of A–$(CH_2)_3$–φ following 0,0 excitation; (a) 2.0 Å monochromator resolution, (b) High resolution scan of the 0,0 region with 0.5 Å monochromator resolution. Expansion conditions were 50 psi Ne and 160 °C sample temperature.

tively attributed to the chain is the 11 cm^{-1} vibration whose 0^0 level dispersed fluorescence progression [Fig. 6(b)] is virtually a mirror image of the 11 cm^{-1} progression observed in excitation (Fig. 5). A band at 77 cm^{-1} may also be due to a chain vibration. (A 77 cm^{-1} mode has been reported in the fluorescence spectrum of anthracene vapor,[29] however, this band is absent in our jet-cooled spectra[15] suggesting that it results from excitation of a sequence or hot band.) The 77 cm^{-1} ground state mode in A–$(CH_2)_3$–φ may correspond to the 69 or 85 cm^{-1} vibrations in the excited electronic state (Table I). It is likely that these modes are due to chain motion on the basis of their absence in anthracene and in comparison with the lowest observed frequencies in the related 1,3-dihalopropanes, namely 82 cm^{-1} (1,3-diiodopropane) and 105 cm^{-1} (1,3-dibromopropane).[30]

The assignment of the weak 189 and 317 cm^{-1} bands in the dispersed fluorescence spectrum of A–$(CH_2)_3$–φ is uncertain. Bree[31] has observed ground state vibrations in anthracene of 179 (weak in dispersed fluorescence) and 166 cm^{-1} (very strong in IR), the latter which he assigns as b_{1u} (in the axis system defined in Ref. 15). A very weak progression of 189, 199, and 209 cm^{-1} is observed in the excitation spectrum of A–$(CH_2)_3$–φ which again has no obvious correspondence with anthracene excited state vibrations. The 317 cm^{-1} transition, likewise, has no obvious correspondence in anthracene nor in the excited state of A–$(CH_2)_3$–φ. Since the 189 and 317 cm^{-1} modes have close counterparts in the 1,3-dihalopropanes, these modes could be assigned to chain vibrations.

The close similarity of the excitation and dispersed fluorescence spectra of A–$(CH_2)_3$–φ with that of anthracene

TABLE II. Assignment of the dispersed-fluorescence spectra of A–$(CH_2)_3$–φ and anthracene.

A–$(CH_2)_3$–φ			Anthracene[b]		
Frequency[a] (cm^{-1})	Relative intensity	Assignment[c]	Frequency (cm^{-1})	Relative intensity	Assignment and symmetry
0	100[d]	origin	0	100	origin
11	48				
21	17				
31	4				
77	5				
			166?		
189	5		179?		
317	4				
386	29		390	45	a_g
593	1				
698	2	386 + 317			
774	4		778	7	2×390
1008	2		1012	2	a_g
1167	9		1165	22	a_g
1254	15		1263	22	a_g
1344	8	1167 + 189			
1407	40		1408	59	a_g
1565	28		1566	31	a_g
1633	10		1643	20	b_{1g}
1739	4	1344 + 386			
1806	10		1797	16	1408 + 390
1950	7	1565 + 386			
2588	3				
2668	4				
2739	2				
2827	10				
2979	8				
3178	3				

[a] Frequencies are reported relative to the 0_0^0 to an accuracy of 5–10 cm^{-1}.
[b] Observed frequencies and intensities are from Ref. 15 and are reported to an accuracy of 5 cm^{-1}.
[c] Symmetries of fundamentals may be associated with the D_{2h} designations of anthracene.
[d] This value encompasses about 20% scattered laser light.

indicates that the bulky propyl-aniline group attached at the 9-position of anthracene does not perturb the planar geometry of the anthryl group significantly in either the ground or the first excited electronic state. This observation also indicates that vibronic excitation in A–$(CH_2)_3$–φ is localized in the anthracene moiety.

C. Energy dependence of the spectra and quantum yields

The dispersed fluorescence spectra of A–$(CH_2)_3$–φ in Fig. 7 allow one to qualitatively examine the extent of intramolecular vibrational redistribution (IVR) and exciplex formation as a function of excess vibrational energy above the 0^0 level. IVR plays a vital role in the conformational change that must occur in A–$(CH_2)_3$–φ to form the exciplex. In the absence of IVR to the propyl group following SVL excitation in the anthryl group, no conformational change in the jet-cooled molecule can occur. The discrete level structure at relatively low energy gives way to a quasicontinuum of states at high energy which may facilitate rapid redistribution of initially excited vibrations into other modes of the molecule (and hence is likened to randomization of energy within a thermal bath[4(b),32]).

Figure 7 clearly shows a distinct broadening of the dispersed fluorescence spectrum at increasing energies. This broadening actually starts at lower excess energies which are not shown. In contrast, broadening in the dispersed fluorescence spectra of anthracene occurs at relatively higher energies.[1] This difference is attributable to the 11 cm^{-1} and other chain modes of A–$(CH_2)_3$–φ which provide a quasicontinuum of bath states at much lower excess energies than in anthracene where similar low frequency modes do not exist. Moreover, the 11 cm^{-1} mode is coupled to the anthracene ring modes as evidenced by the long 11 cm^{-1} progression observed in the excitation spectra (Fig. 2). Hence, IVR from the anthracene ring modes to the chain modes should be very efficient. In Sec. IV C we discuss the ramifications of the 11 cm^{-1} mode by focussing on its involvement with the reaction coordinate through coupling with other chain modes.

The energy dependent dispersed fluorescence spectra (Fig. 7) show in a straightforward manner the extent to which exciplex formation increases with increasing excitation energy. This dependence is represented by the relative quantum yields for exciplex and anthryl-type fluoresence

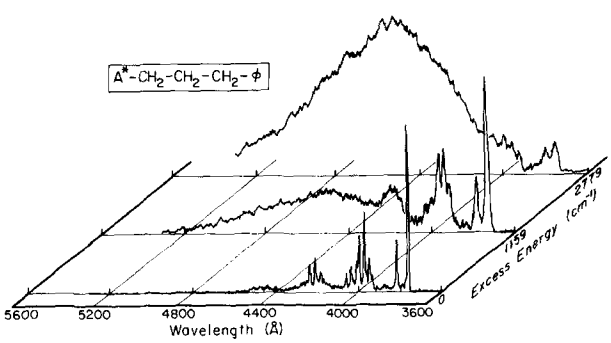

FIG. 7. Dispersed fluorescence spectra of A–$(CH_2)_3$–φ recorded for different excitation energies. Monochromator resolution was 3 Å. Expansion conditions were 50 psi Ne and 160 °C sample temperature.

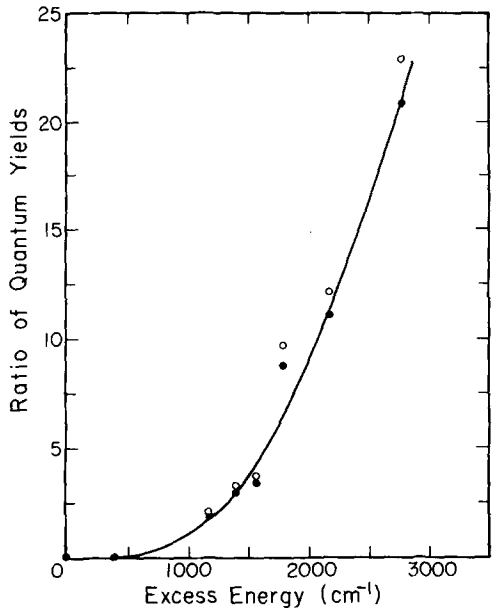

FIG. 8. The ratio of quantum yields Φ_E/Φ_A for exciplex (E) and anthryl-type (A) fluorescence. The raw data (○) have been corrected (●) for the spectral response of the monochromator and PMT. The points are estimated to have about a 10% uncertainty. The curve through the points has been added for clarity.

which we display in Fig. 8. Since the rate of exciplex formation competes with the radiative decay from the anthracene moiety of A–$(CH_2)_3$–φ, these data provide us with important kinetic information regarding exciplex dymamics. We discuss the relative quantum yield determinations in the context of a kinetic model in Sec. IV B, as well as their agreement with the direct time-resolved fluorescence measurements which we describe next.

D. Time-resolved spectra: Decay rates and gated spectra

The fluorescence from the locally excited and exciplex states of A–$(CH_2)_3$–φ were measured in time to determine the decay characteristics as a function of excess vibrational energy E_x. The rapid formation of the exciplex state was measured with our picosecond laser/continuous jet apparatus and the results are displayed in Fig. 9. Both the decay time of the locally excited anthryl state and the rise time of the exciplex state were measured and found to be the same, indicating that no metastable intermediates are involved in the reaction process. This behavior is illustrated in Fig. 10 where we present examples showing the direct correspondence of the locally excited state decay and the exciplex buildup over the entire range of excess energies studied.

The results in Fig. 9 show that a distinct threshold for reaction (exciplex formation) occurs at $E_x \approx 900\ cm^{-1}$ (≈ 2.6 kcal/mol). At lower energies, we measured a 0° level lifetime of 20 ± 1 ns which is very similar to the value of 21.5 ns measured in anthracene.[1] The 11 cm^{-1} progression, however, gave relatively constant lifetimes of 14 ± 1 ns. The lifetimes decreased further to 10 ns for 392 cm^{-1} excitation and remained flat up to the threshold for reaction at $E_x \approx 900$ cm^{-1}. Over this region, IVR is already very efficient (Sec.

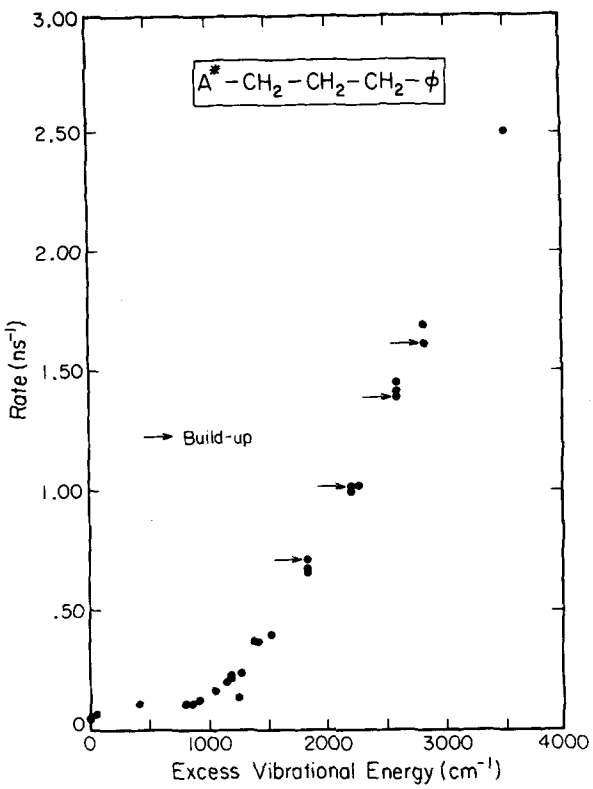

FIG. 9. Observed rates of locally excited anthryl-type fluorescence decay and exciplex fluorescence build-up as a function of excess excitation energy.

III C), hence the nonradiative decay occurs from the bath states. Even so, the nonradiative rate is rather slow ($<5\times10^7$ s^{-1} assuming the 0° to be a radiative lifetime) compared to the sharp increase in the rate due to product formation above the threshold. Similar threshold behavior has been observed in the picosecond time-resolved studies of jet-cooled *t*-stilbene,[5,6] diphenylbutadiene,[7] methylsalicylate,[33] and hydrogen bonded complexes.[34]

The time-resolved spectra of anthracene-like fluorescence exhibited clean single exponential decays. Our exponential fitting program typically gave χ^2 values between 0.90 and 1.10 and standard deviations of 2–3% (Sec. II C). Some fitted curves to experimental data are displayed in Fig. 10. We did observe an interesting example of a nonexponential decay for a very weak excitation line at $E_x = 1210$ cm^{-1}. The best exponential fit for this decay gave an anomalously slow rate as evidenced by the deviant point in Fig. 9. The $E_x = 1210$ cm^{-1} line is associated with a corresponding line displaced 52 cm^{-1} from the 0,0 (Fig. 5). For reasons discussed in Sec. III A 3 this line is a possible candidate for a second conformer of A–$(CH_2)_3$–φ which for geometric reasons is less able to rearrange to the exciplex state. We have located the 1380 + 52 cm^{-1} band and found that the decay of this line is also nonexponential. Unfortunately, this line is extremely weak and is in a region of spectral congestion and broad background fluorescence (see Fig. 2).

It is evident from Fig. 10 that the exciplex is a long-lived state. We have measured the fluorescence lifetimes of the exciplex with our nanosecond laser/pulsed jet system. The results as a function of excess energy are shown in Fig. 11. As expected, the exciplex lifetime is considerably longer in the vapor phase than in solution, although at higher excess energies, it begins to approach solution phase lifetimes (126 ns in isopentane at 20 °C[13(b)]).

In Fig. 12, we compare the total dispersed fluorescence spectra of A–$(CH_2)_3$–φ at $E_x \approx 2800$ cm^{-1} excitation to that of a gated spectrum where only fluorescence emitted within 1.5 ns of laser excitation was collected. At this excess energy, nearly total conversion to the exciplex state occurs (Figs. 7 and 8), yet anthracene-like fluorescence dominates at early times. This testifies to the vastly different emission rates from the locally excited and exciplex states, in accord with our direct time-resolved measurements (Figs. 9 and 11).

IV. DISCUSSION: PHOTOCHEMISTRY AND DYNAMICS

The emphasis of this section follows two major directions; first, the relationship of the observed reaction rates and quantum yields to the dynamics of A–$(CH_2)_3$–φ chain motion, and second, the comparison of the photochemistry in the jet to that in solution to assess the role of the solvent on the dynamics. Picosecond studies in solution[12,13,35] have addressed important questions regarding geometry constraints and solvent dependences. Vapor phase studies,[36,37] including work attending to the time resolution of the fluorescence,[37] have also been reported. However, these experiments were

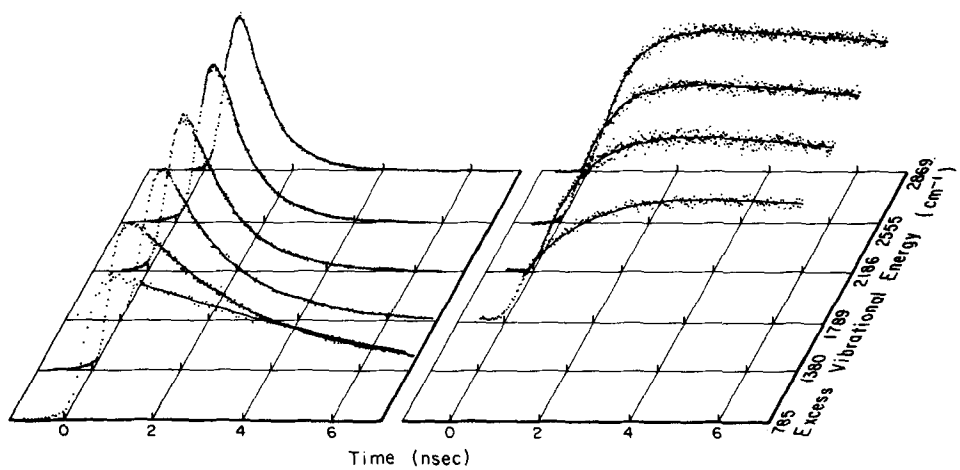

FIG. 10. Observed time-resolved fluorescence spectra for the decay of the initially excited anthryl-type state and the formation of the product exciplex state as a function of excess excitation energy. The curves through the points represent least squares convoluted fits of an exponential function and the system response function.

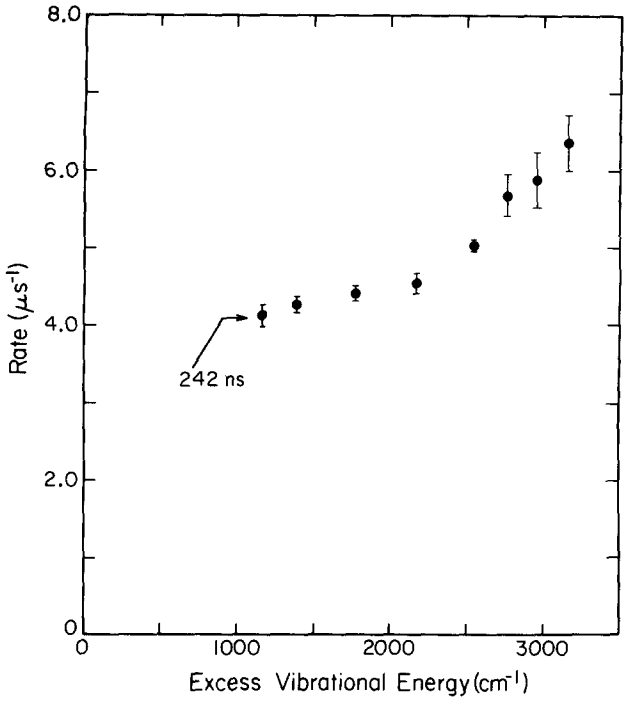

FIG. 11. Measured exciplex fluorescence decay rates λ_2 as a function of initial excess energy in the anthryl moiety. Points represent an average of at least four determinations; the error bars denote the standard deviation. Zero energy is taken to be the 0,0 excitation energy of the locally excited anthryl state of A–$(CH_2)_3$–φ.

restricted to the longer time scale and were encumbered by thermal congestion. The picosecond-jet results reported here will enable us to focus more specifically on the processes that promote reaction. Before examining these points in detail, we shall first highlight the electronic and thermodynamic properties obtained from our jet studies.

A. Electronic and thermodynamic properties

1. Potential energy surface and stabilization energy

We will follow well established steps in evaluating the thermodynamic and kinetic properties of the gas phase exciplex of A–$(CH_2)_3$–φ. Some of these relations are best visualized via the potential energy surface in Fig. 13. We have used the common definition of the reaction coordinate as a distance between the two chromophores.[38–40] Clearly, many chain motions will have components along the reaction coordinate which, in a sense, represents a slice through the potential energy hypersurface containing all vibrational components which contribute to r. In the coming sections we will explore in greater detail a model for the frequencies and pathways of the torsional trajectories along the potential surface for A–$(CH_2)_3$–φ.

In Fig. 13, the excited state surface for exciplex formation may be envisioned as a sum of an attractive interaction due to the charge transfer (CT) interaction (denoted by the basis state, $\psi(A^-\varphi^+)$ and a repulsive interaction due to the usual steric and orbital overlap restrictions [inherent in basis state $\psi(A^*\varphi)$].[41] The basis states will cross and mix to give approximately the excited state reactive surface illustrated in Fig. 13.

The activation energy of 900 cm^{-1} was obtained from our observed energy threshold for exciplex formation (Fig. 9). The energy of the excited electronic state in the extended conformation ($r \approx 5$–6Å) corresponds to the locally excited anthryl-type state, $\psi(A^*\varphi)$, and hence is equivalent to the observed 0° level excitation energy ν_{00}. In so far as the repulsive interactions in the ground (E_R) and excited state ($E_{R'}$) are the same, which is usually taken to be true, then the energy of stabilization ΔH may be expressed as[38–40]

$$-\Delta H = h(\nu_{00} - \nu^E_{\max}) - E_R, \tag{3}$$

where $\nu^E_{\max}$ is the energy at the peak of the exciplex fluorescence. The repulsive energy E_R of the exciplex form of A–$(CH_2)_3$–φ is not known in the vapor phase, however, a value for the intermolecular analog (i.e., anthracene + dimethyl-

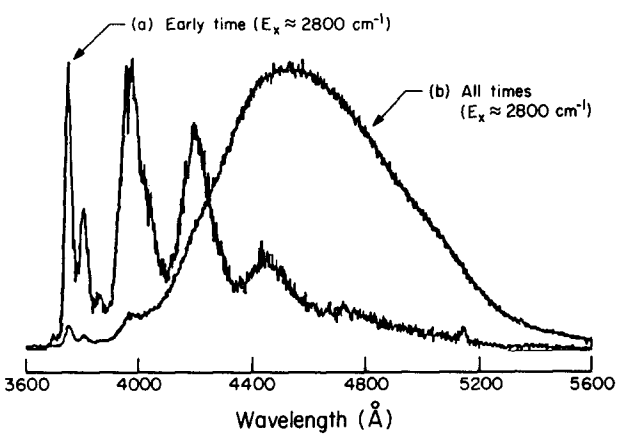

FIG. 12. Temporally gated dispersed fluorescence spectra of A–$(CH_2)_3$–φ for excess excitation energy of 2800 cm^{-1}. Spectra were recorded for emission occurring within (a) 1.5 ns and (b) 1 μs after picosecond laser excitation. Monochromator resolution was 16 Å.

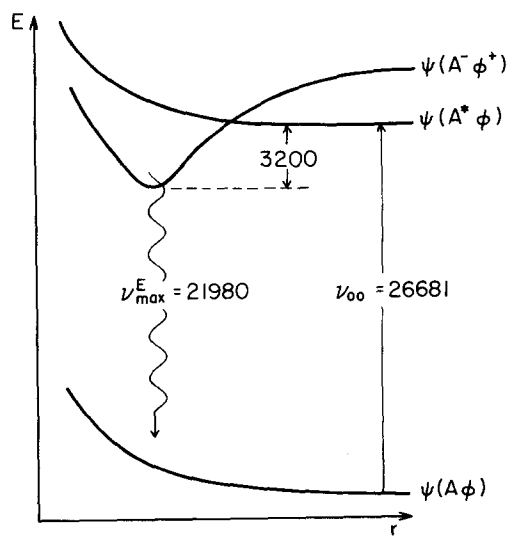

FIG. 13. Simplified potential energy diagram of the ground and excited states of A–$(CH_2)_3$–φ as a function of the distance r between the two chromophores. The attractive interaction is attributed to the pure electron transfer state $\psi(A^-\varphi^+)$, and the repulsive interaction to the locally excited anthryl state $\psi(A^*\varphi)$. The potential surface for the true exciplex eigenstate represents a mixture of the two basis states. We assume that the repulsive interaction in $\psi(A^*\varphi)$ is qualitatively similar to that in the ground state $\psi(A\varphi)$. All energies are expressed in wave numbers.

aniline) has been measured in hexane giving 4.4 kcal/mol.[11] This value compares favorably to other exciplex systems in solution (e.g., 4.4 kcal/mol for pyrene and dimethylaniline[42]) and hence we assume that it approximates the value of E_R in vapor phase A–$(CH_2)_3$–φ. This assumption would hold if: (i) the intramolecular exciplex of A–$(CH_2)_3$–φ can attain the same optimum geometry for stabilization as the corresponding intermolecular exciplex; and (ii) the influence of a nonpolar solvent does not appreciably alter the gas phase repulsive interaction. The first premise is attested to by examining molecular models. The second condition is less certain, however, one would not expect the π orbitals that give rise to the repulsion to be significantly perturbed by a nonpolar solvent. In any case the repulsive energy is not sufficiently large at the equilibrium distance ($r_{eq} = 3$ Å)[39] for the uncertainty in estimating E_R to be sizable. By this approach then, one obtains for the exciplex energy of stabilization the value $\Delta H = -9.2$ kcal/mol. This value compares quite favorably with values obtained for corresponding intermolecular exciplexes in solution (e.g., -12.1 kcal/mol for anthracene-dimethylaniline[11]; and -8.5,[43] -10.2 kcal/mol[44] for anthracene-diethylaniline).

2. Nature of the excited exciplex state

The exciplex electronic state wave function Ψ is commonly represented[39] by a linear combination of the locally excited anthryl-type state, $\psi(A^*\varphi)$, and the electron transfer state, $\psi(A^-\varphi^+)$, (the latter state being the extreme case of CT).

$$\Psi = c_1\psi(A^*\varphi) + c_2\psi(A^-\varphi^+). \tag{4}$$

The energies of the basis states and the amount in which they mix are strongly dependent on the distance r as illustrated in Fig. 13. The other plausible electronic basis states $\psi(A\varphi)$, $\psi(A\varphi^*)$ and $\varphi(A^+\varphi^-)$ are omitted since their energies are quite removed from Ψ. The exciplex fluorescence maximum ν^E_{max}. exhibits a strong dependence on solvent polarity as shown in Fig. 14, which indicates that the exciplex state of A–$(CH_2)_3$–φ is very dipolar. A dipole moment of 15 D has been measured previously for A–$(CH_2)_3$–φ in solution.[10] By applying the same method of analysis to our solution phase (Fig. 14) and jet-cooled spectra, we obtain a similar value of 13 D.

The measured dipole moment alone, however, is not sufficient to determine the coefficients in Eq. (4) unless the dipole moment of the pure $\psi(A^*\varphi)$ and $\psi(A^-\varphi^+)$ states are known. Furthermore, solvent polarity is expected to increase the exciplex dipole moment by stabilizing the CT state. Hence, it is of interest to understand the extensiveness of CT in the isolated molecule where only intramolecular energetics prevail. This problem can be approached by relating the extent of CT [i.e., c_2 in Eq. (4)] to the transition dipole moments of Ψ, $\psi(A^*\varphi)$ and $\psi(A^-\varphi^+)$ to the ground state $\psi(A\varphi)$. The transition dipole moment M in turn, may be determined from the radiative rate constant k_r (Table III) for spontaneous emission, which in a vacuum is given by

$$k_r = \frac{64\pi^4\nu_r^3}{3hc^3}|M|^2, \tag{5}$$

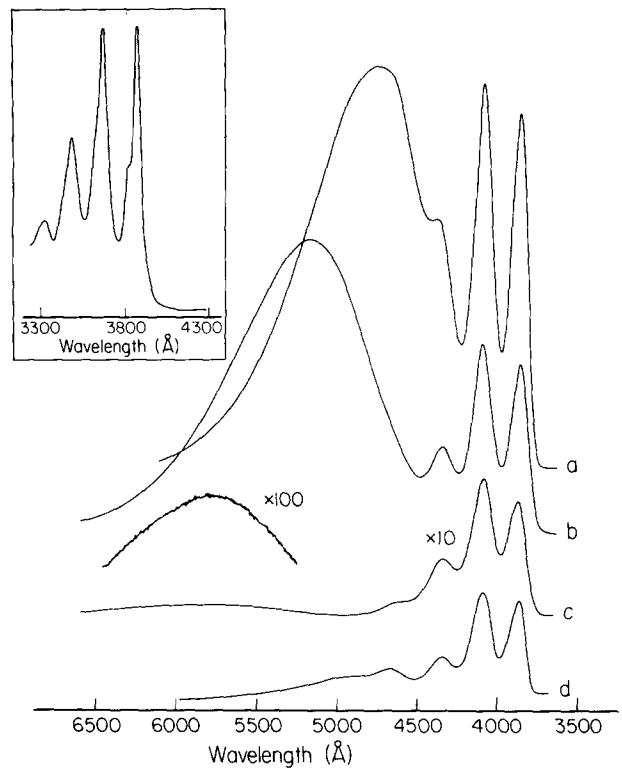

FIG. 14. Solution phase fluorescence spectra of A–$(CH_2)_3$–φ (5×10^{-5} M, 25 °C) in (a) n-hexane ($\epsilon = 1.89$), (b) diethyl ether ($\epsilon = 4.34$), (c) acetone ($\epsilon = 20.7$) and (d) methanol ($\epsilon = 32.6$). The excitation wavelength was 3670 Å from a Hg lamp. The monochromator resolution of 24 Å did not contribute to the observed bandwidths.

where ν_r is the radiative emission frequency and the other terms have the usual meaning. Following Beens and Weller[39] we express the radiative transition moment of the exciplex, M_E by the expression

$$M_E = \langle\Psi|\mu|\psi(A\varphi)\rangle = c_1M_1 + c_2M_2$$
$$= c_1\langle\psi(A^*\varphi)|\mu|\psi(A\varphi)\rangle + c_2\langle\psi(A^-\varphi^+)|\mu|\psi(A\varphi)\rangle. \tag{6}$$

The transition moment M_2 is approximately proportional to the overlap of the acceptor and donor orbitals of A

TABLE III. Kinetic, thermodynamic and optical properties of excited state A–$(CH_2)_3$–φ and related compounds.

	Rate as a function of excess energy	
	1200 cm^{-1}	2800 cm^{-1}
k_e	1×10^8 s^{-1}	1.4×10^9 s^{-1}
k_{-e}	$\leqslant1\times10^5$	$\leqslant1.4\times10^6$
k^A_{nr}	$\leqslant1\times10^8$	$\leqslant3\times10^8$
$\tau^A_r = 20\pm1$ ns[a]		$E_0 = 900$ cm^{-1}
$\tau^E_r = 256\pm10$ ns[a]		$A_e = 1.2\times10^{10}$ s^{-1}
$\nu_{00} = 26681$ cm^{-1}		$\Delta H = 3200$ cm^{-1}
$\nu^E_{max} = 21980$ cm^{-1}		$c_2 = 0.93$
Wavelengths of the 0^0_0 transition		
A–$(CH_2)_3$–φ	3747.7 Å	
9-Hexylanthracene	3730.3	
9-Methylanthracene	3712.0	
Anthracene	3610.7	

[a] The radiative lifetimes τ_r are associated with the 0^0 level fluorescence lifetimes (Sec. IV B2). The quoted uncertainties apply to the fluorescence lifetime measurements and not to the estimated radiative lifetimes.

and φ, respectively,[45,46] and hence falls off rapidly with increasing distance r between the chromophores. Thus M_2 is significantly smaller than the strongly allowed moment M_1. For sufficiently large r the CT state corresponds to a pure electron transfer to form ground electronic state radical ions. This behavior is clearly observed in solution (Fig. 14) where the effect of increasing polarity is to further stabilize the CT state thus quenching the exciplex fluorescence[10,12(b)]. If we ignore M_2 in Eq. (6), then we may express c_1 as

$$|c_1|^2 = \left(\frac{k_r^E}{k_r^A}\right)\left(\frac{\nu^A}{\nu_{\max}^E}\right)^3, \tag{7}$$

where we have distinguished the radiative rate constant and emission frequency for the anthryl-type (A) and exciplex (E) state. Any contribution due to M_2 will have the affect of lowering the value of c_1 determined by Eq. (7). We have also assumed in Eq. (7) that the radiative moments and the Franck–Condon factors for emission in $\psi(A^*\varphi)$ are not significantly altered by the geometry change in A–$(CH_2)_3$–φ. In the isolated molecule, we have estimated k_r^A from the measured 0^0 level lifetime and consequently associate ν^A with the 0_0^0 excitation frequency ν_{00} (Table III). By inserting our measured radiative rate constants and emission frequencies (Table III) for the anthryl and excited states into Eq. (7), we obtain for the coefficients in the linear expansion of Ψ [Eq. (4)], the values $c_1 = 0.37$ and $c_2 = 0.93$. The exciplex fluorescence frequency does not vary with excess energy suggesting that the extent of charge transfer is relatively invariant to the energy of the molecule, at least over the range of energies explored in this study.

The CT character in the exciplex state of A–$(CH_2)_3$–φ may also be estimated roughly from the observed and calculated static dipole moment. We employ a simple point dipole model with charge centered on each aromatic ring of A–$(CH_2)_3$–φ. For a planar separation of 3 Å in the exciplex, we have estimated an average separation from the centers of the aniline ring and the three anthryl rings of 3.7 Å. This leads to a calculated dipole moment of 17.6 D for complete electron transfer [i.e., for $\psi(A^-\varphi^+)$] assuming a homogeneous charge distribution on anthracene. Our value of 13 D indicates that CT is extensive, giving the value $c_2 = 0.86$, in good agreement with our previous determination.

B. Dynamics of product formation

We shall first consider a simple kinetic scheme for analyzing the time resolved and relative quantum yield data. Justifications in applying it to an isolated molecular system will be discussed subsequently.

1. The kinetic model

We adopt the following scheme to describe the kinetics of A–$(CH_2)_3$–φ excited to the first singlet electronic state:

$$\begin{array}{ccc} A^* & \underset{k_{-e}}{\overset{k_e}{\rightleftharpoons}} & E^* \\ \downarrow k_d^A & & \downarrow k_d^E \end{array}$$

A^* and E^* refer to the excited anthryl-type and exciplex states and k_e and k_{-e} are the forward and backward rate constants for exciplex formation. Both states may also decay by radiative k_r and nonradiative k_{nr} processes which we represent by the decay constants k_d^A and k_d^E (where $k_d = k_r + k_{nr}$). The equations describing the populations $N(t)$ of these excited states (assuming a δ-function excitation pulse) are

$$\frac{d}{dt}N_A = -(k_d^A + k_e)N_A + k_{-e}N_E, \tag{8a}$$

$$\frac{d}{dt}N_E = k_e N_A - (k_d^E + k_{-e})N_E. \tag{8b}$$

The solution assuming $N_E(0) = 0$ has been reported before for many systems.[38] The time dependence in terms of fluorescence intensity is given by

$$I_A(t) = k_r^A K\{e^{-\lambda_1 t} + me^{-\lambda_2 t}\}N_A(0) \tag{9a}$$

$$I_E(t) = k_r^E F\{e^{-\lambda_2 t} - e^{-\lambda_1 t}\}N_A(0), \tag{9b}$$

$$K = \frac{\Lambda_1 - \lambda_2}{\lambda_1 - \lambda_2}, \quad F = \frac{k_e}{\lambda_1 - \lambda_2}, \tag{10a}$$

$$m = \frac{\lambda_1 - \Lambda_1}{\Lambda_1 - \lambda_2}, \tag{10b}$$

$$\Lambda_1 = k_d^A + k_e, \tag{10c}$$

$$\Lambda_2 = k_d^E + k_{-e}, \tag{10d}$$

$$\lambda_{1,2} = \tfrac{1}{2}\{(\Lambda_1 + \Lambda_2) \pm [(\Lambda_1 - \Lambda_2)^2 + 4k_e k_{-e}]^{1/2}\}. \tag{10e}$$

We note that Λ_i and λ_i are generally close in value and become equivalent in the limit where $k_{-e} = 0$, a case we discuss shortly.

The absolute quantum yield for fluorescence may be related to the rate constants in our kinetic model by integrating Eq. (9) over all time to give

$$\Phi_A = \frac{1}{N_A(0)}\int_0^\infty I_A(t)dt = k_r^A K\left[\frac{\lambda_2 + m\lambda_1}{\lambda_1\lambda_2}\right], \tag{11a}$$

$$\Phi_E = \frac{1}{N_A(0)}\int_0^\infty I_E(t)dt = k_r^E F\left[\frac{\lambda_1 - \lambda_2}{\lambda_1\lambda_2}\right]. \tag{11b}$$

The experimental measurement of absolute quantum yields requires a count of the number of photons emitted relative to the number of molecules excited. This difficulty, however is avoided when determining relative quantum yields as shown by dividing Eqs. (11a) and (11b) for anthryl-type and exciplex fluorescence,

$$\frac{\Phi_E}{\Phi_A} = \frac{\int_0^\infty I_E(t)dt}{\int_0^\infty I_A(t)dt} = \frac{k_r^E F}{k_r^A K}\left[\frac{\lambda_1 - \lambda_2}{\lambda_2 + m\lambda_1}\right]. \tag{12}$$

The ratio Φ_E/Φ_A can therefore be obtained experimentally by dividing the integrated fluorescence intensities of exciplex and anthryl-type fluorescence. This information, along with our time-resolved measurements, enables us to determine additional rate constants in our kinetic model.

2. Application to experiments

The time-resolved experiments reported here allow us to make the following rigorous assertions for all excess energies E_x studied:

(i) $\lambda_1 \gg \lambda_2$, (13a)

(ii) $\lambda_1 \gg k_{-e}$, (13b)

(iii) $\lambda_1 \approx \Lambda_1$, $\lambda_2 \approx \Lambda_2$. (13c)

The first of these conditions is clearly supported by our measured decay rates for anthryl-type λ_1 and exciplex emission λ_2 which are plotted in Figs. 9 and 11, respectively. The support for the second condition is not as obvious. The value m in Eqs. (9a) and (10b) may be used as a measure of the importance of k_{-e}. For instance, it may be shown using Eqs. (10) that $m = 0$ for $k_{-e} = 0$ and $m = 1$ for $k_{-e} \approx k_e \gg k_d^A, k_d^E$. Equation (9a) indicates that the anthracene-like fluorescence is biexponential, the relative intensity of the slow component given by m. It is evident in Fig. 10, however that all decay curves are fit excellently by a single-exponential function that decays to the baseline by λ_1 and not to a long decay component λ_2 of magnitude m. An upper limit for m is therefore estimated from the baseline uncertainty to be $m \leqslant 0.01$ for all excess energies studied, thus indicating that k_{-e} is negligible. We will discuss a more precise estimate of m shortly. Finally, the relations in condition (iii) follow from conditions (i) and (ii). The small value of m indicates that $k_e \gg k_{-e}$ and consequently $\Lambda_1 \gg k_{-e}, \Lambda_2$. As a result, the first term in the square root of Eq. (10e) dominates the second term, leading to the relations in condition (iii).

Under the conditions in Eq. (13), we may rewrite Eq. (12) as

$$\frac{\Phi_E}{\Phi_A} = \frac{k_r^E k_e}{k_r^A}\left[\frac{1}{\lambda_2 + m\lambda_1}\right], \quad m = \frac{\lambda_1 - \Lambda_1}{\Lambda_1}. \quad (14a)$$

In the limit where the back reaction k_{-e} is negligible [(i.e., $m = 0$)], Eq. (14a) reduces to

$$\frac{\Phi_E}{\Phi_A} = \frac{k_r^E k_e}{k_r^A k_d^E} = \eta k_e. \quad (14b)$$

When η is a slowly varying function of excess energy then Φ_E/Φ_A is proportional to k_e. In this case, the time-resolved measurements (Fig. 9) and the relative quantum yield determinations (Fig. 8) give parallel results.

a. Radiative and nonradiative decays. In A–$(CH_2)_3$–φ, the 0^0 level fluorescence lifetime is 20 ns which is comparable to the value of 21.5 ns measured for the same level in jet-cooled anthracene.[1] These values are very similar to the reported radiative lifetimes of anthracene and derivatives in solution, for instance, anthracene (in ethanol), 20.5 ns[38]; 9-methyl anthracene, 18.3 ns[47]; 9-phenyl anthracene, 16.0 ns[48]; and 9.10-di-n-propyl anthracene, 14.7 ns[49], in various solvents. The exciplex naturally does not form following 0^0 excitation, however, we may obtain an estimate of the radiative lifetime by extrapolating measured fluorescence decay times at higher energies to the 0^0 level of the anthryl-type state. In this manner we obtain a value of 256 ns (cf. Fig. 11). It is worthwhile to comment on the consistency of the estimated radiative lifetimes and the effect of nonradiative decay (by means other than reaction) by relating the time-resolved data to the relative quantum yield results according to Eqs. (14).

In Fig. 15(a), the observed values of Φ_E/Φ_A as a function of E_x are compared to calculated curves based on Eq. (14) and the measured decay rates λ_1 and λ_2 for various values of k_r^A. The calculated curves assume that: (i) back reaction to the locally excited state is negligible (i.e., $k_{-e} = 0$); and (ii) the nonradiative decay rate is given by $\lambda_1 - k_r^A$ below the energy threshold E_α for exciplex formation and does not increase above E_α. Shortly, we will examine the extent of back reaction (k_{-e}) and nonradiative decay (k_{nr}) in more detail.

In spite of the above assumptions, a good fit to the observed relative quantum yield data is obtained in Fig. 15(a) for the radiative lifetimes $\tau_r^A = 20$ ns and $\tau_r^E = 256$ ns of the locally excited and exciplex states, respectively. The small discrepancy between the observed points and the $\tau_r^A = 20$ ns curve may be accounted for if nonradiative decay competes with exciplex formation (k_{nr}^A vs k_e), if exciplex back reaction competes with exciplex fluorescence (k_{-e} vs λ_2) or if the actual radiative lifetime of the exciplex is greater than 256 ns. Since the sum of these effects need not shift the curve in Fig. 15(a) substantially to obtain excellent agreement, it is not likely that any one effect is very significant (although we specifically investigate these possibilities in the following). For instance, a radiative lifetime for the exciplex of $\tau_r^E \approx 280$ ns would lead to excellent agreement between the calculated curve and the observed data. Yet this lifetime corresponds to an exciplex nonradiative rate of only $k_{nr}^E \approx 3 \times 10^5\ s^{-1}$ to account for the estimated 0^0 fluorescence lifetime of 256 ns.

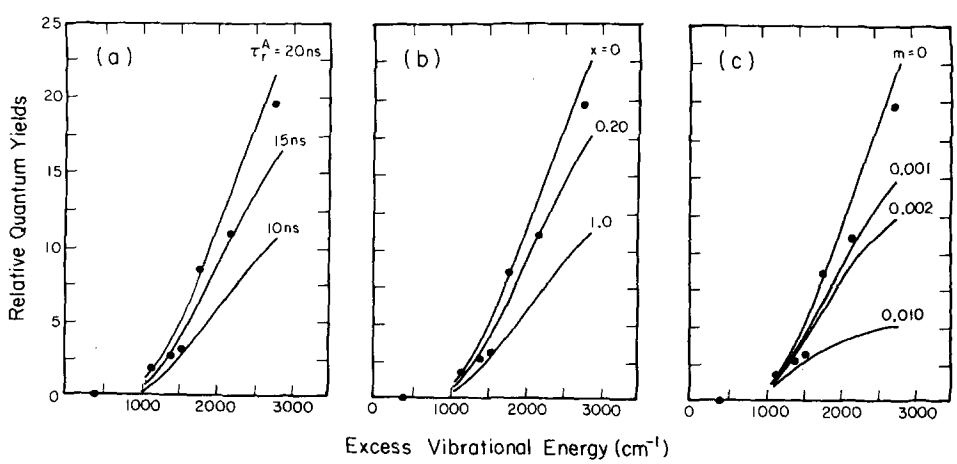

FIG. 15. Calculated vs observed relative fluorescence quantum yields, Φ_E/Φ_A for various kinetic models (see the text) pertaining to (a) radiative lifetime, (b) nonradiative decay and (c) exciplex back reaction. The experimental data (●) are from Fig. 8. Calculated results were obtained using Eq. (14) and the observed decay rates and estimated radiative lifetimes. The curves were drawn through the calculated points.

The effect of a competition between nonradiative decay and exciplex formation is also reflected in the quantum yield ratio Φ_E/Φ_A. For simplicity, we express the excess energy dependent nonradiative rate constant k_{nr}^A as some proportion of k_e, i.e.,

$$k_{nr}^A(E_x) = k_{nr}^A(900) + xk_e \quad \text{for } E_x \geqslant 900\ \text{cm}^{-1}, \tag{15}$$

where $k_{nr}^A(900)$ is k_{nr}^A at the threshold energy $E_x = 900\ \text{cm}^{-1}$ and is given by the measured quantity $\lambda_1 - k_r^A$. Although, there is no reason to expect x to be constant with E_x this model is adequate for assessing the magnitude of k_{nr}^A.

In Fig. 15(b), the best fit to the observed quantum yield data would appear to lie between the curves for $x = 0$ and $x = 0.20$. Since nonzero values for k_{-e} and k_{nr}^E (we assume that they are zero here) would lower the curves in Fig. 15(b) even further, it is unlikely that the nonradiative rate k_{nr}^A is greater than that represented by $x = 0.20$. This conclusion is in accord with results for jet-cooled anthracene. At $E_x = 2800\ \text{cm}^{-1}$, for instance, we estimate $k_{nr}^A \leqslant 3\times10^8\ \text{s}^{-1}$ for A–$(CH_2)_3$–φ compared to $k_{nr} \approx 1.7\times10^8\ \text{s}^{-1}$ for anthracene.[1] The value of x obtained in this way indicates that nonradiative decay does not seriously compete with exciplex formation.

b. Exciplex back reaction. The role of dissociation of the exciplex to the locally excited anthryl state is particularly important from a thermodynamic point of view. The formation of the exciplex requires a certain amount of energy to surmount an activation barrier as evident from the time-resolved data (e.g., Fig. 9). However, the exciplex is *entropically unfavored* compared to the extended conformation of the locally excited state. Hence at higher temperatures, the exciplex should become shorter lived due to dissociation (via k_{-e}) or other channels (via k_{nr}^E).

Under the conditions given by Eq. (13), the square root term in $\lambda_{1,2}$ [Eq. (10e)] may be factored enabling us to express m in Eq. (14a) as

$$m = \frac{k_e k_{-e}}{\lambda_1^2}. \tag{16a}$$

Furthermore, since $\lambda_1 \approx k_e$ above the threshold, we can relate the equilibrium constant K_{eq} to m via the relation

$$K_{eq} = \frac{k_e}{k_{-e}} \approx m^{-1}. \tag{16b}$$

Earlier, we established from the fluorescence decay curves of the locally excited anthryl-type state that $m < 0.01$ (hence $K_{eq} \geqslant 10^2$). The relative quantum yield measurements, however, are far more sensitive to small values of m than the fluorescence decay curves, as is evident in Fig. (15c). This situation is due to the long lifetime of the exciplex which enables slow decay processes to compete effectively with exciplex fluorescence.

The relative quantum yield data provide strong evidence that the exciplex back reaction is very minor. We mention again that other processes which are neglected here (but examined just previously) would act to lower the curves in Fig. 15(c) even further. Consequently, we judge an upper limit for m to be 0.001, in which case $K_{eq} \geqslant 10^3$ [Eq. (16b)]. In terms of the reverse rate constant, one obtains for instance at $E_x = 2800\ \text{cm}^{-1}$ the value $k_{-e} \leqslant 1.4\times10^6\ \text{s}^{-1}$.

3. Justification of simple kinetic model

The kinetics in the present study differ from conventional thermal solution phase experiments in two fundamental ways: (i) laser excitation of jet-cooled molecules allows selective excitation of specific vibrations in the excited electronic state; and (ii) the expanded molecules are collision free and hence subject only to intramolecular interactions. Consequently, a microscopic rate theory is required which describes the kinetics from specifically prepared vibrational states (i.e., $k_e^\nu(E_x)$ for exciplex formation from mode ν with excess energy E_x).

The difference between jet-cooled and vapor phase bulb experiments may be visualized in Fig. 16. An optically active state $|s\rangle$ is excited which in general is not reactive (since the multiple quanta of the reactive modes needed to surmount the activated barrier are rarely optically accessible directly). The $|s\rangle$ state may redistribute energy into a set of isoenergetic bath states $|l\rangle_A$ via the mode dependent rate constant $k_{IVR}^\nu(E_x)$. The density of bath states increases rapidly with E_x in large molecules. As a result, the overall IVR process may become more effective and irreversible; thus the mode selectivity initially imparted to the molecule by laser excitation is lost at sufficiently high energy.

In a thermal system, a large distribution of reactant and product bath states (e.g., $|l\rangle_A$ and $|l\rangle_E$) can interact with each other, thus insuring that an equilibrium is maintained. This condition is not necessarily satisfied when only a narrow band of states is allowed to interact. However, there is a

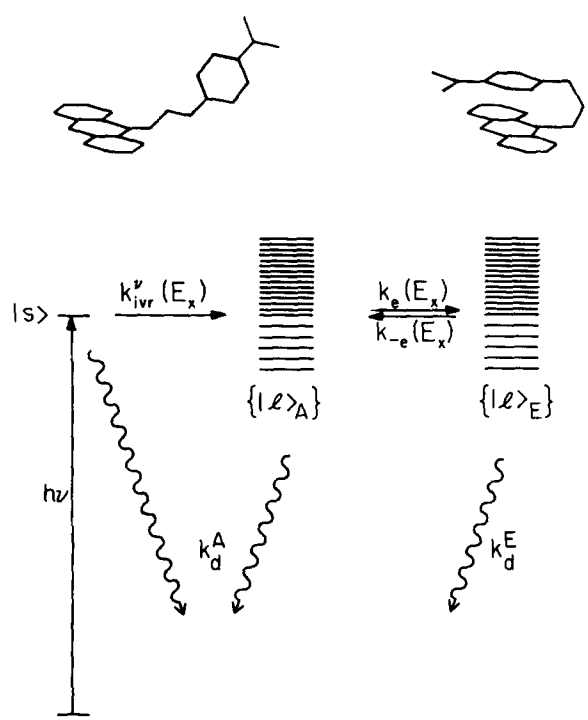

FIG. 16. Representation of the microscopic rate constants for IVR and product formation following mode selective picosecond excitation to the initial state $|s\rangle$. The approximate conformations associated with the reactant and product are illustrated.

correspondence between the quantum mechanical treatment and the kinetic approach.[6,50] Our justification for using the simple kinetic scheme in the above analysis is based on two fundamental assumptions;

(i) Since the $|s\rangle$ state does not lead directly to reaction, we must assume that the reactant bath states $|l\rangle_A$ become populated within the time scale of our experiment (i.e., $k_{\rm IVR} \gg k_e$). This is clearly the case as indicated by the absence of measured mode selective rates. Consistent with this conclusion is the predominance of redistributed (broadened) fluorescence and the absence of resonance fluorescence in the dispersed fluorescence spectra of A–$(CH_2)_3$–φ at excitation energies greater than the 0_0^0 region.

(ii) We assume that there is no quasiperiodic behavior on the timescale of the reaction such as those observed by Felker and Zewail[4(b)] in anthracene. The interactions between $|l\rangle_A$ and $|l\rangle_E$ may be viewed as kinetic in the sense that these two manifolds are reversible. This requires that the density of states within $|l\rangle_A$ and $|l\rangle_E$ at any given excess energy are sufficiently large that redistribution between the manifolds is unrestricted.

C. Intramolecular reaction dynamics

Unimolecular rate theories such as RRKM are statistical in nature and in general consider the limiting case of complete and nonspecific energy randomization by any means, including collisions. However, the dynamics of isolated molecules are not generally statistical (see discussion in Refs. 1 and 2), but may exhibit nonstatistical (or quasiperiodic) behavior in the sense that only a small number of degrees of freedom will mix on a reactive timescale and that recurrences among modes can therefore occur.[51,52] The observed recurrences in anthracene[4] are good examples of this behavior in *large* molecules. For smaller systems, the photodissociation of van der Waals complexes is another example.[53]

We will attempt to unravel the intramolecular reaction dynamics of A–$(CH_2)_3$–φ by appealing to both simple classical and quantum theories of unimolecular reactions. These theories are difficult to apply to complicated systems where the vibrational degrees of freedom and reactive chain modes are not well defined. However a comparison between experiment and theory will allow us to address some important points, such as (i) the number of modes that might be involved in the reaction, which bears on the issue of IVR, (ii) the importance of the torsional motions to the rates and (iii) the effect on the rates due to coupled reactive modes and a multidimensional reaction coordinate.

1. Torsional dynamics

One of the primary considerations in the dynamics of exciplex formation in A–$(CH_2)_3$–φ is in how energy propagates from the optically excited (anthryl) modes into the reactive chain torsions and the concomitant geometric change which enables charge transfer stabilization to occur. The reaction coordinate is a complicated function; as many as four different internal rotations are necessary to project A–$(CH_2)_3$–φ from an extended geometry to the exciplex geometry. It is essential then to characterize the reactive torsional modes (i.e., frequencies, barrier heights) for which spectroscopic information is unavailable. We begin by defining a model in which to calculate the torsional frequencies in A–$(CH_2)_3$–φ.

The periodic potential associated with internal rotation for an N-fold top may be expressed by a series expansion[23] of the form

$$V(\alpha) = \sum_{k,N} \frac{V_{kN}}{2}(1 - \cos kN\alpha), \tag{17}$$

where V_{kN} represents the amplitude (or barrier) for each periodic component N. Values of k allow for higher orders of perturbations (e.g., anharmonicities). For our purposes, it is sufficient to retain only the $k = 1$ (harmonic) term. The frequency of a harmonic torsion in the most stable conformation is known[23] to give

$$\nu_T(cm^{-1}) = \sum_N \frac{N}{2\pi}\left(\frac{V_N}{2I_R}\right)^{1/2}, \tag{18}$$

where I_R is a reduced moment of inertia for a given torsion. This equation is similar to Eq. (2) in Sec. III A2.

For rotation of the mth top, the reduced moment may be determined from the method of Pitzer and Gwinn[54]

$$I_{Rm} = I_m\left(1 - \sum_{i=1}^{3} I_m \lambda_{mi}^2 / I_i\right), \tag{19}$$

where I_m is the moment of inertia of the mth top, I_i the moment of inertia of the whole molecule about the ith principal axis, and λ_{mi} is the direction cosine between the axis of the mth top and the ith principal axis. Equation (19) is an exact expression for a single top and is usually a satisfactory approximation for a molecule with several tops. For instance, Eq. (19) has been used to describe the rotational isomerism of a 1,3-dibromopropane,[55] a molecule not unlike A–$(CH_2)_3$–φ. Equation (19), however, becomes cumbersome when the principle axes are not known, particularly for large asymmetric molecules such as A–$(CH_2)_3$–φ. The reduced moment of inertia for torsional motion may also be defined by the simple expression

$$I_R = \frac{I_1 I_2}{I_1 + I_2}, \tag{20}$$

where I_1 and I_2 are the moments of inertia about the torsional axis of the two parts of the molecule involved in the motion. Both methods of determining I_R gave similar results, although, for A–$(CH_2)_3$–φ Eq. (20) proved more convenient.

We describe the internal rotations in A–$(CH_2)_3$–φ by the following angles

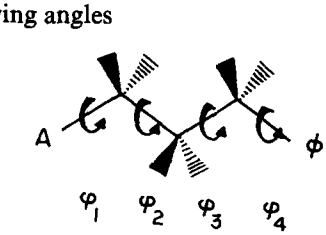

The torsions represented by φ_2 and φ_3 involve two threefold asymmetric tops giving a threefold potential for internal rotation. The φ_1 and φ_4 torsions involve the interaction of a threefold asymmetric top with the twofold plane of an aro-

matic system giving an overall sixfold potential. The interaction of the aromatics with the adjacent chain hydrogens, however, is slight as indicated by the mere 5 cm^{-1} barrier to internal rotation in toluene,[24] hence, we assume that the φ_1 and φ_4 torsions have simple twofold potentials. The different conformational energies and the asymmetric tops in A–$(CH_2)_3$–φ introduce several terms into the potential energy equation [Eq. (17)]. However, since we lack adequate information regarding these properties we consider just the leading term representing the dominant periodicity in $V(\alpha)$ (i.e., $N = 2$ for φ_1 and φ_4 and $N = 3$ for φ_2 and φ_3). This will tend to underestimate the torsional frequencies but not by an amount considered serious for these approximate calculations.

We report the results of our calculations in Table IV. The input barriers V_N were based on measured or calculated values in analogous systems. For the individual torsions about φ_2 and φ_3 we used $V_3 \approx 1200$ cm^{-1} from the calculated barrier in 1,3-dibromopropane,[56] whereas for φ_1 and φ_4 we estimated barriers of $V_2 \approx 1000$ and 600 cm^{-1}, respectively, based on calculated and measured barriers in alkyl benzenes.[26] Our calculated torsional frequencies apply to the extended (i.e., *tt*, Fig. 17) conformation of A–$(CH_2)_3$–φ. We calculated ν_T for other conformations about φ_2 and φ_3 and for variations in the aromatic rotations, however only minor differences were encountered. As a check of our simple model, we calculated ν_T for the $\varphi_2 = \varphi_3$ torsion in 1,3-dibromo- and 1,3-diiodopropane assuming a barrier of $V_3 = 1200$ cm^{-1}. As expected for this simple model, the calculated values are smaller than the observed values (Table IV). The inclusion of higher order periodic components V_N on the potential energy surface has the effect of increasing the calculated frequencies as indicated by Eq. (18). However, for the purposes of this discussion and for the RRKM calculations to follow (Sec. IV C3) the simple model achieves sufficient accuracy.

2. Reaction rates

We begin by applying a simple theory to describe the excess energy dependence of the rates. Recently, it was shown that an activation[3,51] type rate equation could be applied to isolated molecules to describe the rate constant at a given excess energy provided that an effective temperature is defined according to the number of vibrational modes involved. The expression is given by

TABLE IV. Calculated torsional frequencies.

A–$(CH_2)_3$–φ			1, 3-*diX* Propane			
	Calc	Obs		Calc	Obs[c]	
φ_1	8	11[a]				
φ_2	28			63[b]	105	(X = Br)
φ_3	15		$\varphi_{2,3}$	51	82	(X = I)
φ_4	21					

[a] Tentative assignment, Sec. III A 2.
[b] $\varphi_2 = \varphi_3$ for the symmetry substituted 1, 3-dihalopropanes.
[c] Reference 30.

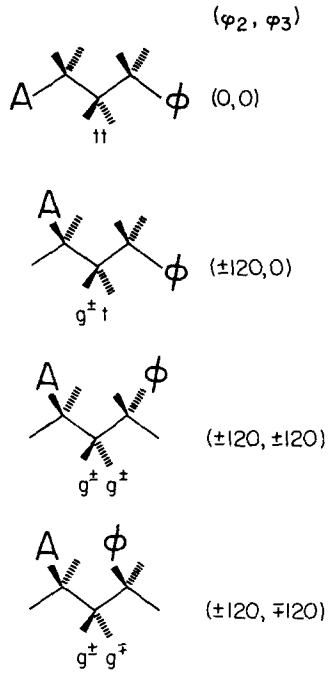

FIG. 17. Schematic representation of the major conformations of A–$(CH_2)_3$–φ. A threefold torsional potential is assumed for rotation about φ_2 and φ_3. The sense of rotation is defined about the torsional axis viewed from the central carbon. The signs + and − are arbitrary as long as account is taken of the relative sign of rotation about the two bonds (i.e., $g^+g^- = g^-g^+$).

$$k = Ae^{-nE_0/E_x} = Ae^{-E_0/kT_{\text{eff}}}, \tag{21}$$

where n is the number of effective modes, E_0 is the threshold energy, and A is the preexponential frequency factor.

The measured rate constants, k_e for exciplex formation were analyzed via Eq. (21). Using our value of $E_0 = 900$ cm^{-1} (Fig. 9), we obtained a very linear ln k plot yielding the values $A_e = 1.2 \times 10^{10}$ s^{-1} and $n = 6.3$ (Fig. 18). Eq. (21) has also been found to describe other reactive systems in supersonic jets.[3,6,57] It is worth noting that the small frequency factor determined here agrees to within the experimental uncertainty of that observed for the related intermolecular exciplex system anthracene + dimethylaniline in hexane.[11]

For the sake of comparison, we have also analyzed the time-resolved data to the RRK expression

$$k = A\left[\frac{E - E_0}{E}\right]^{n-1} \tag{22}$$

for various values of E_0 in the vicinity of the observed value $E_0 = 900$ cm^{-1} (Fig. 19). For $E_0 = 900$ cm^{-1}, we obtained $n = 4.6$ and $A_e = 0.82 \times 10^{10}$ s^{-1}, in reasonable agreement with the results derived from the effective temperature relation [Eq. (21)].

The small frequency factor that we have observed is common to most exciplex[11] and excimer[38(b)] systems and is usually attributed to the negative entropy associated with exciplex formation. For example, in systems with well defined temperature (i.e., solution or thermal bulbs), it follows[38(b)] from the Arrhenius equations for k_e and k_{-e} and the relation $\Delta G = -RT \ln K$ that

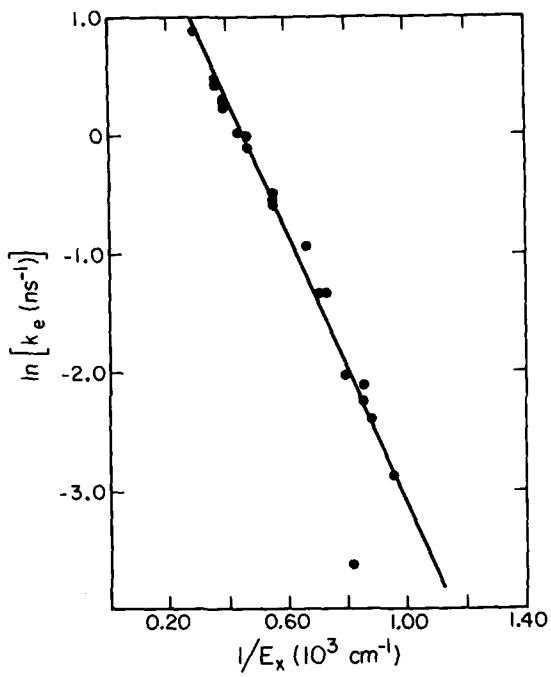

FIG. 18. Effective temperature analysis of reaction rates as a function of E_x. For the observed energy barrier $E_0 = 900\ \text{cm}^{-1}$, a linear logarithmic fit to Eq. (21) was obtained giving the values $A_e = 1.2\times10^{10}\ \text{s}^{-1}$ and $n = 6.3$.

$$\frac{A_e}{A_{-e}} = e^{\Delta S/R}. \tag{23}$$

In isolated isoenergetic molecules it is the energy and not the temperature that is well defined and hence the concept of entropy must be examined in a different context. We consider this point by using an energy specific RRKM model shortly. A small frequency factor, however, might also be expected in situations involving non-adiabatic surface crossings and/or multimode reaction coordinates. The latter case is believed to be especially pertinent to the exciplex kinetics, which we examine in greater detail next.

3. RRKM calculations and multidimensional reactive surface: A model

Having calculated reasonable values for the torsional frequencies and estimated barriers to internal rotation in A–$(CH_2)_3$–φ we proceed to a model which relates the multidimensional reactive surface and the coupled torsional motions involved in exciplex formation to the observed energy dependent rates.

The formation of a stable exciplex state from an extended conformation involves many torsions. The basic motions involve internal rotations about φ_2 and φ_3 to bring the chromophores to their closest approach and rotation about φ_1 and φ_4 to attain coplanarity for maximum orbital overlap. To simplify the picture, we focus on the more critical torsions φ_2 and φ_3. In accord with threefold tops, we allow for 120° steps in these coordinates. Consequently, four conformations may be envisioned which are illustrated in Fig. 17. We adopt the label convention of Flory.[22] The estimated energies and barriers for the various conformers in both the ground and excited electronic state are diagrammed in the potential surface in Fig. 20. The ground state surface of A–$(CH_2)_3$–φ approximates that of 1,3-diiodopropane and pentane except for the repulsive $g^{\pm}g^{\mp}$ for which the energy was estimated in Sec. IV A1. (The $g^{\pm}g^{\pm}$ conformer is similar in energy to $g^{\pm}t$ and hence is excluded for convenience.) The

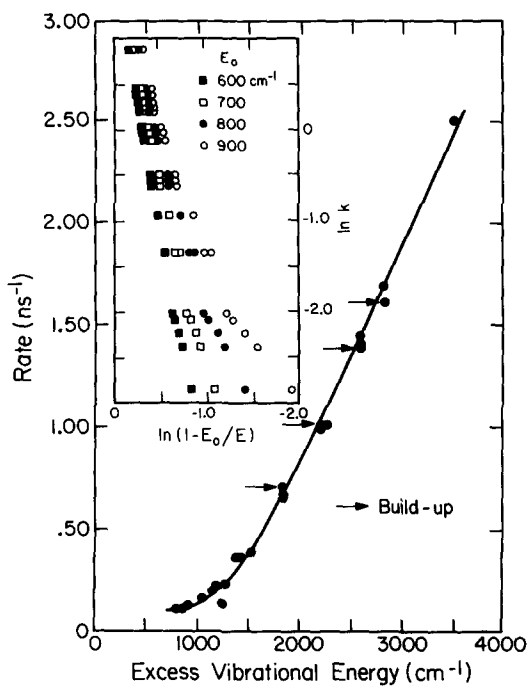

FIG. 19. RRK analysis of reaction rates as a function of E_x. The arrows designate rates measured for the build-up of the product. The results for $E_0 = 900\ \text{cm}^{-1}$ were $A_e = 0.82\times10^{10}\ \text{s}^{-1}$ and $n = 4.6$. The insert shows logarithmic plots of the experimental data for various values of E_0.

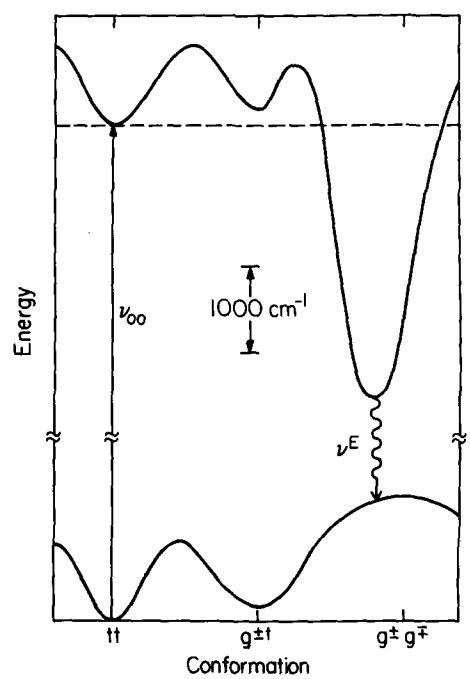

FIG. 20. Potential energy diagram for various conformers. ν_{00} and ν^E denote, respectively, the frequencies of the 0,0 excitation of the anthryl moiety and the exciplex fluorescence. Notice that the optimum exciplex geometry deviates slightly from a true $g^{\pm}g^{\mp}$ configuration.

excited electronic surface is assumed to exhibit similar properties to that of the ground state with the exception of the $g^{\pm}g^{\mp}$ conformer which forms a stable exciplex (see also Fig. 13).

The conventional potential energy diagram in Fig. 20 illustrates the energy relations between conformers. However, as illustrated, it considers just one trajectory consisting of consecutive torsional steps leading to reaction. The true motions in A–$(CH_2)_3$–φ are probably more varied, involving correlated motion among the torsions as well as nonreactive trajectories. To illustrate this situation, we have recast the excited electronic state potential into a $2D$ contour diagram in Fig. 21 involving the major torsions φ_2 and φ_3. The conformational changes in A–$(CH_2)_3$–φ may now be visualized in terms of trajectories on this surface. For example, independent torsional motion is described by trajectories consisting of vertical and horizontal steps, whereas concerted torsional motion is represented by trajectories in all directions.

Figure 21 enables one to visualize how the involvement of several modes along the reaction coordinate affect the rate of reaction compared to a simple single mode situation (e.g., bond dissociation). For a one dimensional reaction coordinate (i.e., the diagonal trajectory from [0,0] to $[\pm 120 \mp 120]$, for instance), the only trajectory is reactive. When two vibrations participate in the reaction, however, an added dimension of nonreactive trajectories is introduced even when the reactive modes are fully activated as is evident in Fig. 21. It follows then that the greater the number of coupled reactive modes (e.g., four torsions in A–$(CH_2)_3$–φ), the greater is the space of nonreactive trajectories. One outcome for such behavior might be reaction rates which exhibit an unusually small frequency factor.

We have investigated the effects of multiple reactive modes in A–$(CH_2)_3$–φ using RRKM theory and a model for coupled rates. For the RRKM calculations we followed the procedure outlined by Khundkar *et al.*[57] RRKM theory holds that

$$k(E_x) = \frac{N^{\#}(E^+)}{h\rho(E_x)}, \tag{24}$$

where $N^{\#}(E^+)$ is the total number of quantum states in the transition state in the energy region $E^+ = E_x - E_0$ (where E_0 is the barrier to reaction) and $\rho(E_x)$ is the density of states of the reactant at excess energy E_x. No thermal averaging is required for our system.

The RRKM calculations employed the Hase–Bunker program[58] for computing $k(E_x)$. Certain features of this program have been discussed previously.[57] The total effective vibrational degrees of freedom were approximated by using the calculated vibrational modes of anthracene,[59] 1,3-diiodopropane[60] and the calculated (or observed) torsions in Table IV. We assumed that the reactant and transition state vibrations are equivalent and harmonic with the exception of the reactive mode(s). The activation energies used in the calculations were estimated from conformational studies of molecules analogous to A–$(CH_2)_3$–φ (e.g., dihalopropanes,[55,56,61] pentane,[22] and alkylbenzenes[26]) and are incorporated into the model surface in Fig. 21.

RRKM theory can only accommodate a one-dimensional reaction coordinate (and hence only one reactive mode). We have, therefore, adopted a simple model for coupled reaction rates based on Fig. 21. Three situations were investigated.

(i) Concerted motion: A conventional one-dimensional reaction coordinate involving the initially excited conformer $[\varphi_2,\varphi_3] = [0,0]$ and the exciplex conformer $[-120, +120]$ (see also Fig. 17). This would entail the concerted motion of the torsions about φ_2 and φ_3.

(ii) Consecutive motion: A two-dimensional reaction coordinate involving only stepwise torsional motion. This requires that the molecule go through an intermediate conformer (either $[-120,0]$ or $[0, +120]$) before forming the exciplex.

(iii) Same as (ii) except that trajectories involving all conformers in Fig. 21 are considered. This situation allows for the possibility of nonreactive trajectories.

RRKM rate constants connecting all adjacent conformers (rate matrix) were calculated as a function of excess energy E_x and the resulting set of coupled equations of motion for all conformers were solved numerically. The calculated rates for exciplex formation under the conditions described above are compared with the observed rates in Fig. 22.

The calculated rates in all cases are substantially greater than the observed rates. It is not certain, however, how much significance may be attached to the absolute scale for the calculated rates in view of the uncertainties involved in characterizing many of the vibrations in A–$(CH_2)_3$–φ. However, the relative rates obtained for the three models are very informative.

The calculated results confirm our intuitive expectation that the greater the number of possible intermediates and nonreactive trajectories, the slower will be the rate of product formation. Models (i) to (iii) obey relatively linear acti-

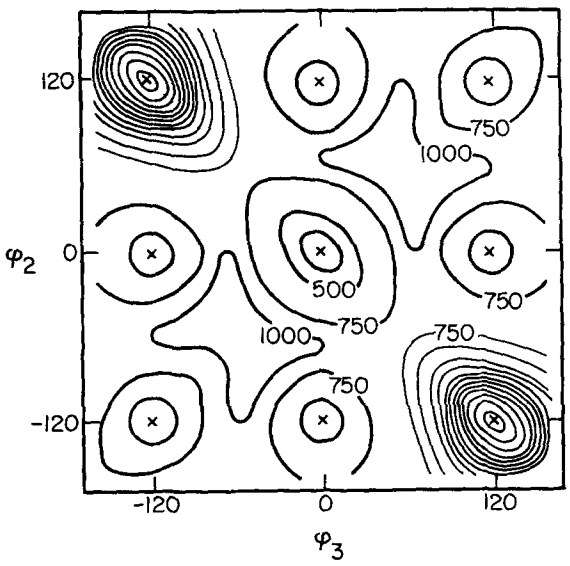

FIG. 21. Approximate two-dimensional excited state potential energy surface for torsional motion about the axes φ_2 and φ_3. Each contour represents 250 cm^{-1} of energy. Minima are indicated by $\times$. Note the deep well corresponding to the exciplex geometry at $[\pm 120, \mp 120]$. The initially excited conformation is [0,0] which represents the most stable conformer in the ground electronic state.

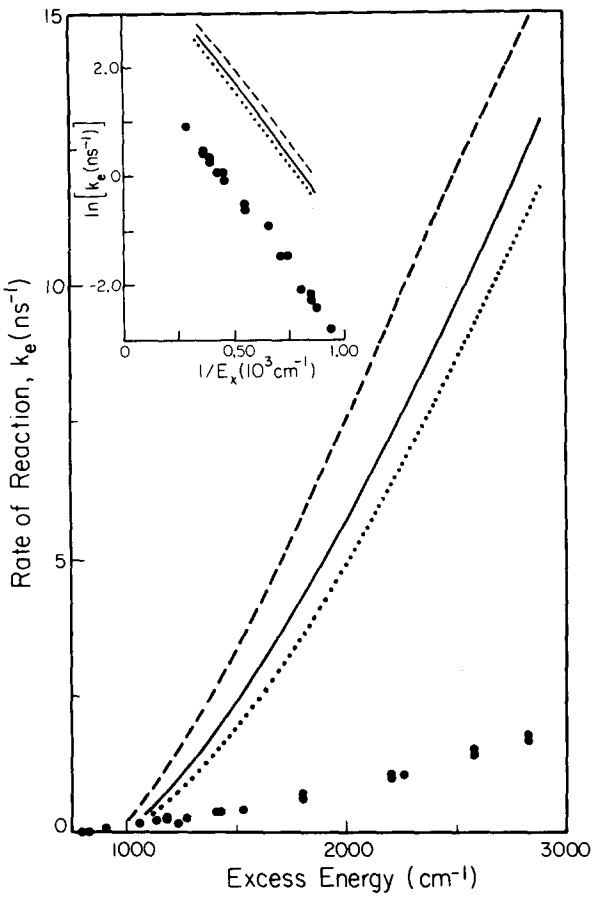

FIG. 22. Calculated vs observed rates for exciplex formation assuming various models for a multidimensional reaction coordinate; (- - -) 1-dimensional reactive surface with concerted torsional motion; (—) two-dimensional surface with consecutive torsional motion and reactive trajectories only; and (· · ·) two-dimensional surface with consecutive torsional motion and nonreactive trajectories; (●) observed data. The insert illustrates analysis of calculated and observed results using Eq. (21) and the measured value of $E_0 = 900\ cm^{-1}$.

vation log dependences [Eq. (21), Fig. 22] that are parallel to the observed data. The preexponential frequency factors A_e obtained in this manner were 1.1×10^{11}, $9.4\times10^{10}\ s^{-1}$, and $8.0\times10^{10}\ s^{-1}$, respectively. According to this trend, the use of a potential surface that also considers the importance of the φ_1 and φ_4 torsions on the reaction coordinate should lead to better agreement with the observed value of $A_e = 1.2\times10^{10}\ s^{-1}$.

Complete agreement between theory and experiment is probably not possible with the above model since we have not adequately accounted for the entropic destabilization of the exciplex in the RRKM calculations. A multidimensional reaction coordinate may be considered to contribute an entropy effect in the sense that the greater the number of accessible states (e.g., conformers) the more entropically unfavored is any one state. What has not been considered here, however, are any differences in entropy that may exist between the different conformers due to geometry.

The entropy associated with an isoenergetic reaction (i.e., the energy of the reactant and product are the same) is different from that encountered in a thermal reaction where energy due to exothermicity can be dissipated. The equilibrium constant for forward and backward reaction may be written using the energy specific RRKM expression in Eq. (24) to give

$$K = \frac{k_e}{k_{-e}} = \frac{\rho_E}{\rho_A} = e^{\Delta S/R}. \tag{25}$$

It is assumed that the transition state for k_e and k_{-e} are the same and that the reactant and product have the same energy. The terms ρ_A and ρ_E refer to the density of states of the anthryl-type reactant and the exciplex product, respectively, at a given excess energy E_x. We note that ΔS is therefore also energy dependent. ΔS may be estimated if we assume that the vibrational level structure in the reactant and product are the same and calculate the density of states according to the method described earlier. Choosing $E_x = 2000\ cm^{-1}$ and an energy of stabilization of $\Delta H = 3200\ cm^{-1}$ (Table III) one obtains the result $\Delta S = 22$ e.u. The large entropy impedes back reaction even though sufficient energy is available. In a thermal system, the product energy can relax and hence ΔS is smaller. However, the back reaction must then overcome an energy barrier.

Equation (25) does not consider other entropy effects such as those due to geometry constraints (i.e., ΔS_{geo}). For exciplex formation this consideration is very important, hence we express the observed equilibrium constant K_{obs} as

$$K_{obs} = e^{\Delta S_{obs}/R} = e^{(\Delta S + \Delta S_{geo})/R}. \tag{26}$$

In Sec. IV B2, it was determined that $K_{obs} \geqslant 10^3$. If we assume that the equality holds, then one obtains the values, $\Delta S_{obs} = 14$ e.u. and $\Delta S_{geo} = -8$ e.u. Although these results are rough estimates, they are consistent with the entropy destabilization expected for a folding of the molecule to form the product exciplex. In fact, a value of $\Delta S_{geo} \approx -4$ e.u. would explain the discrepancy between the observed and RRKM rates (Fig. 22). Unfortunately, no entropy determinations of intramolecular exciplexes resembling A–$(CH_2)_3$–φ could be found. The entropies for intermolecular exciplexes are expected to be much larger since a more drastic geometry change takes place. Thus, for the sake of comparison we cite the value of $\Delta S_{obs} = -25$ e.u. determined for anthracene + dimethylaniline in cyclohexane.[11] Since this is a thermal system, the observed entropy may be attributed to the geometry change.

4. Role of the solvent

Intramolecular exciplex formation requires extensive internal rotation to achieve the essential geometry change. One might, therefore, expect the reaction rates to be noticeably impeded in solution compared to the vapor phase. Eisenthal and co-workers[12(b)] showed that the rate of exciplex formation for A–$(CH_2)_3$–φ is viscosity dependent with time constants for reaction ranging from 1.4 (isopentane) to 3.8 ns (tetradecane). It is not known, however, the extent to which the fastest observed rate is slowed by solvent drag. To address this point, we have calculated the rate of exciplex formation expected for a vapor phase sample of A–$(CH_2)_3$–φ in thermal equilibrium at the experimental temperature[12(b)] of 20 °C. The thermal rate constant, $k_e(T)$, was related to our measured excess energy dependent rate constants $k_e(E_x)$ via a Boltzmann distribution. The procedure has been described

previously[57] and is given by the expression

$$k_e(T) = \frac{1}{Q}\int_0^\infty k(E_x)\rho(E_x)e^{-E_x/kT}dE_x. \quad (27)$$

The density of states $\rho(E_x)$ and the partition function Q were computed using the calculated modes of anthracene,[59] 1,3-diodopropane[60] and the observed and calculated torsional modes in Table IV. Our approximate model for the density of states (i.e., harmonic overtones and exclusion of the modes in the dimethylaniline chromophore φ) underestimates the actual value of $\rho(E_x)$ and Q. The calculated rate is therefore considered to be a lower limit. We obtained the value k_e (20°) $= 1.8\times10^9\ s^{-1}$ (i.e., $\tau = 540$ ps) indicating that even at low viscosity, the solvent strongly impedes the geometry change required for exciplex formation.

What is perhaps surprising about the intramolecular exciplex formation in solution is that pure single-exponential behavior was observed.[12,13] In solution, the rates of large amplitude motions such as internal rotations are usually governed by viscous drag, particularly if bulky groups are involved. Hence, the end-to-end encounter probability of the two chromophores in A–$(CH_2)_3$–φ is diffusional and therefore not necessarily exponential. One suggestion for the observed exponential formation of exciplex in solution[12(b)] is that low frequency global motions[62] may account for this behavior. However, the nature of these motions are not precisely known. Another mechanism may be postulated based on the present model if we assume that torsions φ_2 and φ_3 which bring the chromophores to their closest approach, are not sufficient alone to promote reaction, but that rotation about φ_1 and φ_4 are also necessary to achieve coplanarity of the aromatics. Consequently, many nonreactive end-to-end trajectories may occur before the geometry of A–$(CH_2)_3$–φ becomes suitable for reaction. We may view this behavior schematically:

$$tt \quad g^{\pm}g^{\mp} \rightarrow \text{exciplex}.$$

The interconversion between the various conformers of A–$(CH_2)_3$–φ, via torsional chain motion about φ_2 and φ_3, may be diffusional in solution and hence nonexponential. However, exciplex formation from the critical $g^{\pm}g^{\mp}$ conformer may occur through aromatic rotation about φ_1 and φ_4 which may be less diffusional and more exponential in nature.

V. SUMMARY AND CONCLUSION

We have investigated the picosecond state-selective dynamics and photochemistry of the molecule

$$A\text{–}CH_2\text{–}CH_2\text{–}CH_2\text{–}\phi$$

under collision-free conditions in a supersonic jet. The principal intent of this work was to directly measure the rate of product (charge transfer or exciplex) formation resulting from IVR to the reactive chain vibrations following mode specific excitation of the anthryl vibrations. In this regard we obtained the rates, relative quantum yields and dispersed fluorescence spectra as a function of vibrational energy above the 0^0 level. Excitation spectra were recorded to assign the vibrations in the first excited electronic state of A–$(CH_2)_3$–φ and to compare with anthracene, 9-methylanthracene and 9-hexylanthracene. The major conclusions drawn from this work are summarized as follows:

(i) The rate of IVR is faster than the reaction rate at all excess energies studied. This was evident from the lack of mode-selective rates at any given energy and consistent with the dispersed fluorescence and excitation spectra.

(ii) The photochemical rate of product (exciplex) formation vs excess energy above the 0^0 level was observed to have a threshold at $E_x \approx 900\ cm^{-1}$ (2.6 kcal/mol). An analysis of the experimental results by an effective temperature approach led to a preexponential frequency factor of $A_e \approx 1.2\times10^{10}\ s^{-1}$. We further considered the effects of chain dynamics in promoting the reaction by adopting a model for a multidimensional reaction coordinate using an RRKM scheme. Four torsions were identified as critical to reaction and their frequencies calculated using a harmonic theory. One of these was assigned to the optically active 11 cm^{-1} mode observed in both the ground and excited state. The effects on the calculated rates were examined for coupled torsional motion by *concerted* vs *consecutive* pathways as well as the extent of nonreactive trajectories involving the reactive modes.

(iii) Various thermodynamic properties of the reaction in the jet have been elucidated, e.g., $\Delta H = -9.2$ kcal/mol for exciplex stabilization, $c_2 = 0.93$ for the extent of charge transfer in the exciplex and $13D$ for the excited state dipole moment. We observed no evidence for the dissociation of the product exciplex back to the initially excited anthryl state ($k_{-e} \leqslant 0.001k_e$) although the exciplex lifetime does vary with excess energy.

(iv) The time-resolved data on jet-cooled A–$(CH_2)_3$–φ were compared to solution phase results to examine the role of the solvent. The static thermodynamic properties of A–$(CH_2)_3$–φ are similar in both phases. However, the dynamics leading to product formation differ substantially. The shortest measured reaction lifetime for exciplex formation of A–$(CH_2)_3$–φ in solution is 1.4 ns[12(b)]. However, based on a density of states model and our measured energy selective rates, we calculated a lifetime of 540 ps for the same thermal system in the vapor phase. This lifetime is comparable to that measured in the jet at an excess energy of $\approx 3000\ cm^{-1}$. Apparently, even low viscosity solvents can significantly impede large amplitude motions such as the torsional modes in A–$(CH_2)_3$–φ.

ACKNOWLEDGMENTS

We gratefully acknowledge the support of this work by the National Science Foundation. We are especially thankful to Prof. D. A. Evans for the use of his laboratory facilities and to Mr. Carl Illig for considerable advice in the synthesis of the model compound A–$(CH_2)_3$–φ. Finally, we wish to thank the organic chemistry group at the University of Bordeaux for providing us with a sample of 9-hexylanthracene.

APPENDIX: SYNTHESIS OF A–$(CH_2)_3$–φ

The following efficient new scheme was developed to synthesize A–$(CH_2)_3$–φ;

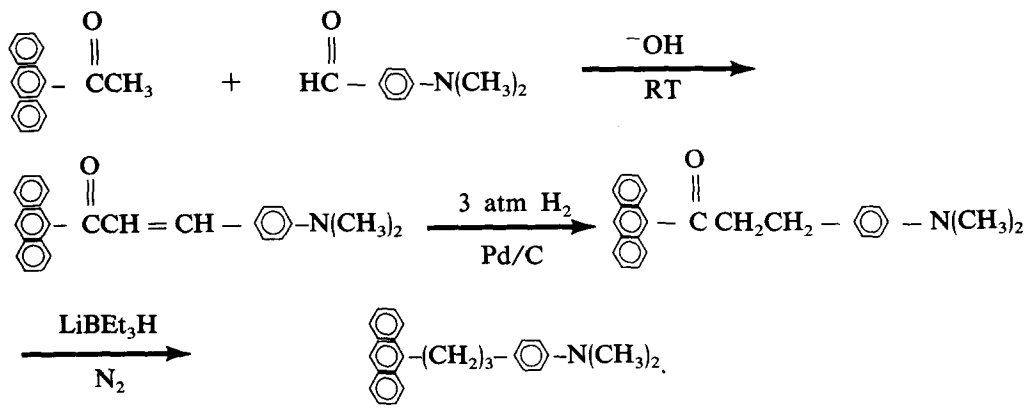

1-(9-anthroyl)-2-(4-N,N-dimethylaniline) ethylene. 10g (46 mmol) of 9-acetyl anthracene was dissolved in 300 ml of 95% ethanol with the help of a steam bath. 25 ml of 3 M NaOH was then added. To this was added a solution of 7 g 4-*N,N*-dimethylamino benzaldehyde in 50 ml 95% ethanol and stirred. Orange precipitate began to appear in ~ 1 h, however, the reaction required two days for completion. The yellow/orange precipate was filtered, washed with water and dried on a rotary evaporator, a vacuum line, and a vacuum oven containing P_2O_5. Yield 95%; mp 188–190: ir 1585, 1510 cm^{-1}; NMR ($CDCl_3$) δ 2.90 (*s*,6), 6.5 (*d*,2), 7.09 (*s*,2), 7.23 (*d*,2), 7.40 (*m*,4), 7.95 (*m*,4), 8.45 (*s*,1).

1-(9-anthroyl)-2-(4-N,N-dimethylaniline) ethane. 4 g (11.4 mmol) portions of 1-(9-anthroyl)-2-(4-N,N-dimethylaniline) ethylene were added to 200 ml of acetone containing 200 mg of 5% or 10% Pd on *C* catalyst and reduced on a Parr hydrogenator over 3 atm H_2 for 12 hr. The reaction mixture was filtered through a fine fritted filter packed with ~ 1 in. of Cellite to remove the catalyst, then rotovapped and vacuum dried. The oily product was sufficiently pure (~95% by NMR and tlc) to be used directly in the next reaction. Yield 90%; ir 1690, 1610, 1515 cm^{-1}; nmr ($CDCl_3$) δ 2.83 (*s*,6), 3.24 (*q*,4), 6.64 (*d*,2), 7.13 (*d*,2), 7.40 (*m*,4), 7.65 (*m*,2), 7.95 (*m*,2), 8.40 (*s*,1).

1-(9-anthroyl)-3-(4-N,N-dimethylaniline) propane. 10 g (28.5 mmol) of 1-(9-anthroyl)-2-(4-*N,N*-dimethylaniline) ethane was added to a 150 ml solution of 1 M $LiBEt_3H$ (superhydride) in THF, stirred at RT for 30 min and refluxed for 2 h under an atmosphere of N_2. The workup of the reaction mixture is as follows; 200 ml of 3 M NaOH was added very slowly with a drop funnel. 100 ml of methanol was then added, followed by the dropwise addition of 30 ml of 30% H_2O_2. Rigorous fizzing accompanies these steps. The solution was refluxed for 3 h after which an additional 25 ml of 30% H_2O_2 was added. The solution was allowed to sit for 12 h after which another 30 ml of 30% H_2O_2 was added. The aqueous layer was washed with ether, combined with the organic layer, dried over $MgSO_4$, filtered, rotovapped and vacuum dried. 9.8 g of crude product (~75% pure by NMR) was recovered. The desired material was purified by flash chromatography using 37–53 μm silica gel and a 55:45 by volume mixture of CH_2Cl_2:hexane, followed by two recrystallizations in ethanol. mp 101.5–102.5; NMR ($CDCl_3$) δ 2.10 (*m*,2), 2.80 (*t*,2), 2.92 (*s*,6), 3.55 (*t*,2), 6.67 (*d*,2), 7.12 (*d*,2), 7.35 (*m*,4) 7.92 (*m*,2), 8.12 (*m*,2), 8.25 (*s*,1).

Anal. Calc for $C_{25}H_{25}N$:C, 88.45; H, 7.42; N, 4.13. Found: C, 88.16; H, 7.42; N, 4.10.

[1] W. R. Lambert, P. M. Felker and A. H. Zewail, J. Chem. Phys. **81**, 2209 (1984).
[2] W. R. Lambert, P. M. Felker and A. H. Zewail, J. Chem. Phys. **81**, 2217 (1984).
[3] (a) A. H. Zewail, Discuss. Faraday Soc. **75**, 315 (1983); (b) A. H. Zewail in *Picosecond Phenomena III*, edited by K. Eisenthal, R. Hochstrasser, W. Kaiser, and A. Laubereau (Springer, New York, 1982), p. 184.
[4] (a) W. R. Lambert, P. M. Felker, and A. H. Zewail, J. Chem. Phys. **75**, 5958 (1981); (b) P. M. Felker and A. H. Zewail, Chem. Phys. Lett. **102**, 113 (1983).
[5] J. A. Syage, W. R. Lambert, P. M. Felker, A. H. Zewail, and R. M. Hochstrasser, Chem. Phys. Lett. **88**, 266 (1982).
[6] J. A. Syage, P. M. Felker, and A. H. Zewail, J. Chem. Phys. (to be published).
[7] J. F. Shepanski, B. W. Keelan, and A. H. Zewail, Chem. Phys. Lett. **103**, 9 (1983).
[8] J. A. Syage, F. Al Adel, and A. H. Zewail, Chem. Phys. Lett. **103**, 15 (1983).
[9] P. M. Felker, J. A. Syage, W. R. Lambert, and A. H. Zewail, Chem. Phys. Lett. **92**, 1 (1982).
[10] T. Okada, T. Fujita, M. Kubota, S. Masaki, N. Mataga, R. Ide, Y. Sakata, and S. Misumi, Chem. Phys. Lett. **14**, 563 (1972).
[11] M-H. Hui and W. R. Ware, J. Am. Soc. **98**, 4718 (1976).
[12] (a) T. J. Chuang, R. J. Cox, and K. B. Eisenthal, J. Am. Chem. Soc. **96**, 6828 (1974); (b) Y. Wang, M. C. Crawford, and K. B. Eisenthal, *ibid.* **104**, 5874 (1982); (c) H. Staerk, R. Mitzkus, H. Meyer, and A. Weller, Appl. Phys., B **30**, 153 (1983).
[13] (a) M. K. Crawford, Y. Wang, and K. B. Eisenthal, Chem. Phys. Lett. **79**, 529 (1981); (b) Y. Wang, M. K. Crawford, and K. B. Eisenthal, J. Phys. Chem. **84**, 2696 (1980); (c) K. Gnädig and K. B. Eisenthal, Chem. Phys. **46**, 339 (1977).
[14] B. W. Keelan, J. A. Syage, J. F. Shepanski, and A. H. Zewail, *International Conference Proceedings of Laser 83* (in press).
[15] W. R. Lambert, P. M. Felker, J. A. Syage and A. H. Zewail, J. Chem. Phys. **81**, 2195 (1984).
[16] (a) A. V. Bree and S. Katagiri, J. Mol. Spectrosc. **17**, 24 (1965); (b) A. Bree, S. Katagiri, and S. R. Suart, J. Chem. Phys. **44**, 1788 (1966); (c) R. M. Macnae and K. Sauer, *ibid.* **53**, 2805 (1970); (d) G. J. Small, *ibid.* **52**, 656 (1970); (e) Ch. Jung, A. Kawski, and M. I. Zukowska, Z. Naturforsch. Teil. A **34**, 557 (1979).
[17] J. B. Hopkins, D. E. Powers, and R. E. Smalley, J. Chem. Phys. **72**, 5039 (1980).
[18] (a) T. F. Schatzki, J. Polym. Sci. **57**, 496 (1962); (b) Polym. Preprints, **6**, 646 (1965).
[19] (a) J. Skolnick and E. Helfand, J. Chem. Phys. **72**, 5489 (1980); (b) **77**, 5714 (1982).
[20] (a) L. Monnerie and F. Ge'ny, J. Chim. Phys. **66**, 1691 (1969); (b) B. Valeur, J.-P. Garry, F. Ge'ny and L. Monnerie, J. Polym. Sci. Polym. Phys. Ed. **13**, 667 (1975).
[21] G. Herzberg, *IR and Raman Spectroscopy of Polyatomic Molecules* (Van Nostrand Reinhard, New York, 1945), Chap. III.

[22]P. J. Flory, *Statistical Mechanics of Chain Molecules* (Interscience, New York, 1969).
[23]A. V. Cunliffe, in *Internal Rotations in Molecules*, edited by W. J. Orville Thomas, (Wiley, New York, 1974), Chap. 7.
[24](a) H. P. Rudolph, H. Dreizler, A. Jaeschke, and P. Wendling, Z. Naturforsch. Teil. A **22**, 940 (1967); (b) W. A. Kreiner, H. D. Rudolph, and B. T. Tan, J. Mol. Spectrosc. **48**, 86 (1973).
[25]R. K. Harris and M. Thorley, J. Mol. Spectrosc., **42**, 407 (1972).
[26](a) F. C. Brickwedde, M. Moskow, and R. B. Scott, J. Chem. Phys. **13**, 547 (1945); (b) M. Camail, A. Proutiere, and H. Bodot, J. Phys. Chem. **79**, 1966 (1975); (c) P. Scharfenberg, B. Rozsondai and I. Hargittai, Z. Naturforsch. Teil. A **35**, 431 (1980); (d) D. P. Poshkus and A. J. Grumadas, J. Chromatogr. **191**, 169 (1980).
[27]Work in progress.
[28](a) M. Van der Auweraer, A. Gilbert, and F. C. De Schryver, J. Am. Chem. Soc. **102**, 4007 (1980); (b) F. Meeus, M. Van der Auweraer, and F. C. De Schryver, Chem. Phys. Lett. **74**, 218 (1980).
[29]S. O. Mirumyants, E. A. Vanbynkov, Yu. S. Demchuk, and Yu. S. Nagulin, Opt. Spektrosk. **36**, 90 (1974).
[30]J. Thorbjørnsrud, O. H. Ellestad, P. Klaboe, and T. Torgrimsen, J. Mol. Struct. **15**, 61 (1973).
[31]A. Bree and R. A. Kydd, J. Chem. Phys. **48**, 5319 (1968).
[32](a) J. W. Perry, N. F. Scherer, and A. H. Zewail, Chem. Phys. Lett. **103**, 1 (1983); (b) N. F. Scherer, J. F. Shepanski, and A. H. Zewail, J. Chem. Phys. **81**, 2181 (1984).
[33]P. M. Felker, W. R. Lambert, and A. H. Zewail, J. Chem. Phys. **77**, 1603 (1982).
[34](a) P. M. Felker and A. H. Zewail, Chem. Phys. Lett. **94**, 448, 454 (1983); (b) P. M. Felker and A. H. Zewail, J. Chem. Phys. **78**, 5266 (1983).
[35](a) M. Migita, T. Okada, N. Mataga, N. Nakashima, K. Yoshihara, Y. Sakata, and S. Misumi, Chem. Phys. Lett. **72**, 229 (1980); (b) K. Egawa, N. Nakashima, N. Mataga, and Ch. Yamanaka, *ibid.* **8**, 108 (1971); (c) Y. Taniguchi and N. Mataga, *ibid.* **13**, 596 (1972); (d) T. J. Chuang and K. B. Eisenthal, J. Chem. Phys. **59**, 2140 (1973); (e) **62**, 2213 (1975).
[36](a) S. Hirayama, G. D. Abbott, and D. Phillips, Chem. Phys. Lett. **56**, 497 (1978); (b) S. Hirayama, *ibid.* **63**, 596 (1979); (c) S. Okajima and E. C. Lim, *ibid*, **70**, 283 (1980); (d) J. Prochorow, S. Okajima, and E. C. Lim, *ibid*, **66**, 590 (1979).
[37](a) D. V. O'Connor, L. Chewter, and D. Phillips, J. Phys. Chem. **86**, 3400 (1982); (b) M. Itoh, T. Kotani, and Y. Hanashima, Chem. Phys. Lett. **75**, 307 (1980); (c) M. Itoh, Y. Hanashima, and I. Hanazaki, J. Phys. Chem. **87**, 569 (1983).
[38](a) J. B. Birks, *Photophysics of Aromatic Molecules* (Wiley, New York, 1970), Chaps. 7 and 9, pp. 311, 360.
[39]H. Beens and A. Weller in *Organic Molecular Photophysics, II* edited by J. B. Birks (Wiley, New York, 1975), Chap. 4.
[40]B. Stevens, Adv. Photochem. **8**, 161 (1971).
[41]*The Exciplex*, edited by M. Gordon and W. R. Ware (Academic, New York, 1975).
[42]H. Nakashima, N. Mataga, and C. Yamanaka, Int. J. Chem. Kinet. **5**, 833 (1973).
[43]H. Beens, H. Knibbe, and A. Weller, J. Chem. Phys. **47**, 1183 (1967).
[44]H. Knibbe, D. Rehm, and A. Weller, Ber. Bunsenges, Phys. Chem. **73**, 839 (1969).
[45](a) N. Mataga, T. Okada, and N. Yamamoto, Chem. Phys. Lett. **1**, 119 (1967); (b) N. Mataga and T. Kubota, *Molecular Interactions and Electronic Spectra* (Marcel Dekker, New York, 1970).
[46](a) S. T. Cheung and W. R. Ware, J. Phys. Chem. **87**, 466 (1983); (b) D. V. O'Connor and W. R. Ware, J. Am. Chem. Soc. **101**, 121 (1979).
[47](a) J. Rice, D. B. McDonald, L-K Ng, and N. C. Yang, J. Chem. Phys. **73**, 4144 (1980); (b) S. Schoof, H. Güsten and C. von Sonntag, Ber. Bunsenges. Phys. Chem. **82**, 1068 (1978).
[48]I. B. Berlman, *Handbook of Fluorescence Spectra of Aromatic Molecules*, (Academic, New York, 1965).
[49](a) N. S. Bazilevskaya, L. A. Limareva, A. S. Cherkasov, and V. I. Shirokov, Opt. Spectrosc. **18**, 202 (1965); (b) N. S. Bazilevskaya and A. S. Cherkasov, *ibid.* **18**, 77 (1965).
[50]F. Lahmani, A. Tramer, and C. Tric, J. Chem. Phys. **60**, 4431 (1974).
[51]A. H. Zewail, Laser Chem. **2**, 55 (1983).
[52]D. W. Noid, M. L. Koszylowski, and R. A. Marcus, Annu. Rev. Phys. Chem. **32**, 267 (1981).
[53](a) R. E. Smalley, D. H. Levy, and L. Wharton, J. Chem. Phys. **64**, 3266 (1976); (b) R. E. Smalley, L. Wharton, and D. H. Levy, Acc. Chem. Res. **10**, 139 (1977).
[54]K. S. Pitzer and W. D. Gwinn, J. Chem. Phys. **10**, 428 (1942).
[55]M. A. Cochran, A. S. Gilbert, J. Greer, and R. A. Pethrick, Spectrochim. Acta. Part A **32**, 859 (1976).
[56]P. E. Farup and R. Stølevik, Acta. Chem. Scand. Ser. A **28**, 680 (1974).
[57]L. R. Khundkar, R. A. Marcus, and A. H. Zewail, J. Phys. Chem. **87**, 2473 (1983).
[58]W. L. Hase and D. L. Bunker, Program QCPE-234, Caltech, Pasadena.
[59]K. Ohno, J. Mol. Spectrosc. **77**, 329 (1979).
[60]G. A. Crowder and S. Ali, J. Mol. Struct. **25**, 377 (1975).
[61]A. Y. Meyer and N. Ohmichi, J. Mol. Struct. **73**, 145 (1981).
[62]M. Fixman, J. Chem. Phys. **72**, 1504 (1980).